

1 Measuring the iron content of 2 dopaminergic neurons in substantia 3 nigra with MRI relaxometry

4 Malte Brammerloh^{abc}, Markus Morawski^d, Isabel Weigelt^d, Tilo Reinert^{ac},
5 Charlotte Lange^{ac}, Primož Pelicon^e, Primož Vavpetič^e, Steffen Jankuhn^c, Carsten
6 Jäger^a, Anneke Alkemade^f, Rawien Balesar^f, Kerrin Pine^a, Filippos Gavriilidis^a,
7 Robert Trampel^a, Enrico Reimer^a, Thomas Arendt^d, Nikolaus Weiskopf^{act}, and
8 Evgeniya Kirilina^{aj†}

*For correspondence:

mbrammerloh@cbs.mpg.de (MB)

†These authors contributed equally
to this work

9 ^aDepartment of Neurophysics, Max Planck Institute for Human Cognitive and Brain
10 Sciences, Stephanstr. 1a, 04103 Leipzig, Germany; ^bInternational Max Planck Research
11 School on Neuroscience of Communication: Function, Structure, and Plasticity; ^cFelix
12 Bloch Institute for Solid State Physics, Faculty of Physics and Earth Sciences, Leipzig
13 University, Linnéstr. 5, 04103 Leipzig, Germany; ^dPaul Flechsig Institute of Brain Research,
14 University of Leipzig, Liebigstr. 19, 04103, Leipzig, Germany; ^eJožef Stefan Institute,
15 Jamova 39, SI-1000 Ljubljana, Slovenia; ^fIntegrative Model-based Cognitive Neuroscience
16 Research Unit, University of Amsterdam, Amsterdam, Nieuwe Achtergracht 129B, 1001
17 NK Amsterdam, The Netherlands; ^jCenter for Cognitive Neuroscience Berlin, Free
18 University Berlin, Habelschwerdter Allee 45, 14195, Berlin, Germany

19

20 Abstract

21 In Parkinson's disease, the depletion of iron-rich dopaminergic neurons in *substantia nigra's*
22 nigrosome 1 precedes first motor symptoms by two decades. Monitoring this neuronal depletion at
23 an early disease stage is needed for diagnosis and treatment monitoring. Magnetic resonance
24 imaging (MRI) is particularly suitable for this task due to its sensitivity to tissue iron. However, the
25 mechanisms of MRI contrast in *substantia nigra* are not well understood, hindering the
26 development of specific biomarkers. We showed that the dominant contribution to the effective
27 transverse MRI relaxation rate R_2^* in nigrosome 1 originates from iron accumulated in the
28 neuromelanin of dopaminergic neurons. We linked R_2^* quantitatively to the product of cell density
29 and local iron concentration in dopaminergic neurons, combining quantitative 3D iron histology,
30 biophysical modeling, and quantitative MRI on *post mortem* brain tissue. This knowledge opens an
31 avenue for monitoring neuronal iron and density *in vivo* and may be applied to detect early
32 neurodegeneration in Parkinson's disease.

33

34 Introduction

35 Pathologic iron accumulation is a biomarker and potential cause of several neurodegenerative
36 diseases, among them Parkinson's disease (PD) (Ward *et al.*, 2014). In PD, iron overload in dopamin-
37 ergic neurons (DN) in *substantia nigra* (SN) is followed by their depletion (Zucca *et al.*, 2017), starting
38 in neuron-rich nigrosome 1 (N1) (Damier *et al.*, 1999a,b). This neuronal depletion precedes first mo-
39 tor symptoms of PD by nearly two decades and remains mostly undiscovered until the majority of

40 DN are irreversibly lost (Agid, 1991). Therefore, *in vivo* methods capable of monitoring iron content
41 in DN and DN loss are highly desired for early diagnosis and monitoring of potential treatments.

42 Magnetic Resonance Imaging (MRI) promises to provide such information, as it allows a unique,
43 noninvasive glimpse into the cellular iron distribution (Sulzer *et al.*, 2018; Edwards *et al.*, 2018;
44 Fukunaga *et al.*, 2010; Schenck and Zimmerman, 2004). Several MRI parameters change in the SN of
45 PD patients. Among them are the effective transverse relaxation time T_2^* and therefore the intensity
46 in T_2^* -weighted images (T_2^* -WI) (Kwon *et al.*, 2012), local magnetic susceptibility (Langkammer *et al.*,
47 2016), and the image intensity in an MRI sequence sensitive to neuromelanin, the main iron chelator
48 in DN (Sasaki *et al.*, 2006; Isaías *et al.*, 2016; Cheng *et al.*, 2019). Most strikingly, the so-called
49 *swallow tail*, an elongated structure with prolonged T_2^* often interpreted as N1 (Blazejewska *et al.*,
50 2013; Lehericy *et al.*, 2014; Péran *et al.*, 2010; Schwarz *et al.*, 2014; Cheng *et al.*, 2019), disappears
51 in the SN of PD patients. In a population of patients with motor symptoms, the absence of
52 this feature can be used to diagnose PD with a sensitivity of 100% and a specificity of 95% or
53 higher (Cosottini *et al.*, 2014; Schwarz *et al.*, 2014). This high diagnostic power at a late disease
54 stage suggests that MRI-based PD biomarkers may also be useful for early stage diagnostics.

55 Despite the wide-spread use of MRI for imaging SN, the mechanisms underlying MRI contrasts
56 in SN and especially in the nigrosomes are not well understood. While multiple tissue components
57 of SN induce transverse MRI relaxation, iron is thought to be causing most of it in the myelin-
58 poor nigrosomes (Lee *et al.*, 2018). Several studies performed careful qualitative comparisons
59 between MRI and histology on *post mortem* tissue from PD patients and controls unaffected by
60 neurodegenerative disease (Blazejewska *et al.*, 2013; Sasaki *et al.*, 2006; Lee *et al.*, 2018, 2020;
61 Rutledge *et al.*, 1987). They demonstrated that nigrosomes show contrast to the surrounding tissue
62 in SN. Iron, accumulated in neuromelanin in DN and in the iron storage protein ferritin in glial
63 cells, was hypothesised to impact relaxation decisively (Zecca *et al.*, 2004a; Lee *et al.*, 2018, 2020).
64 However, a quantitative link between MRI parameters in SN, SN's cellular composition, and the
65 cellular iron distribution is still missing. Quantitative information about the iron distribution in
66 different cellular populations in SN is largely lacking (Morawski *et al.*, 2005; Reinert *et al.*, 2007,
67 2006). It is not clear if iron in neurons or glial cells, in ferritin or in neuromelanin dominates the
68 iron-induced MRI contrast in SN, particularly in the nigrosomes.

69 A strong quantitative link between MRI parameters and the cellular iron distribution would
70 greatly enhance the specificity and interpretability of MRI biomarkers. The theory describing MRI
71 relaxation induced by magnetic perturbers, such as iron, on the microscopic scale (Kiselev and
72 Novikov, 2018; Yablonskiy and Haacke, 1994; Gagnon *et al.*, 2015) demonstrated great potential:
73 It describes the effective transverse relaxation time of blood (Kiselev and Novikov, 2002, 2018),
74 explains how the signal depends on the blood oxygenation level (Gagnon *et al.*, 2015; Uludağ *et al.*,
75 2009; Ulrich and Yablonskiy, 2016), and using this theory blood vessel sizes can be measured (Tro-
76 près *et al.*, 2001). Until now, it has not been applied to describe the relaxation resulting from
77 iron-rich cells in the nigrosomes.

78 Herein, we close this gap by building and validating a fully quantitative biophysical model of iron-
79 induced relaxation in the nigrosomes of SN. We quantified the cellular iron distribution between DN
80 and other tissue components in the nigrosomes, combining 3D quantitative iron histology based on
81 proton-induced x-ray emission microscopy (PIXE) and histochemistry on *post mortem* human tissue.
82 We quantified the predominant contribution of iron to the transverse and the effective transverse
83 relaxation rates $R_2 = 1/T_2$ and $R_2^* = 1/T_2^*$ in the nigrosomes, using ultra-high resolution quantitative
84 MRI and chemical tissue iron extraction. Combining the obtained knowledge with biophysical
85 modeling of the MRI signal, we demonstrated that iron accumulated in DN causes the major part
86 of iron-induced relaxation in N1 and pinned down an appropriate model for this contribution.
87 Extrapolating the biophysical model, we showed that assessing the iron content in DN *in vivo* is
88 within reach of state-of-the-art MRI. The established quantitative link between MRI parameters and
89 the cellular iron distribution constitutes a crucial step towards the *in vivo* characterisation of DN.

90 Theoretical Considerations

91 Tissue iron contributes to the transverse and effective transverse relaxation rates through processes
92 that can be categorized into molecular interactions on the nanoscale and dephasing due to a
93 heterogeneous cellular iron distribution on the microscale (Eqs. (1), (2)) (*Kiselev and Novikov, 2018*).
94 In order to interpret relaxation rates in SN and to link them to the cellular iron distribution, we
95 estimated the impact of different relaxation processes from first principles and determined the
96 most relevant ones. A detailed theoretical treatise of iron-induced relaxation rates and an analytical
97 description of spin echo (SE) and gradient echo (GE) decays induced by nano- and microscale
98 processes are presented in the Materials and Methods section. The most important results for
99 interpreting iron-induced MRI parameters and guiding the experiments are summarized here.

100 Remarkably, the relaxation processes on the nanometer and micrometer scale manifest them-
101 selves differently in R_2^* and R_2 .

102 Molecular interactions with iron on the nanoscale induce very fast fluctuations of the water
103 proton Larmor frequency, resulting in transverse relaxation. Such processes impact R_2^* and R_2
104 equally, due to effective diffusion averaging over the nanoscale distances between the iron-storage
105 complexes. The nanoscale contributions to relaxation rates are determined by the average tissue
106 content of iron stored in ferritin and neuromelanin ($\bar{c}_{\text{Fe,NM}}$ and $\bar{c}_{\text{Fe,FT}}$, respectively; Eq. (3)) and are
107 not dependent on the cellular iron distribution.

108 In contrast, the heterogeneous cellular distribution of iron on the microscale results in a per-
109 turbation of the Larmor frequency around iron-rich tissue components (such as iron-rich cells or
110 fibers), which are not fully averaged out by water diffusion. Therefore, R_2^* is impacted stronger than
111 R_2 , up to an exclusive contribution to R_2^* in the static dephasing limit for large or well separated
112 iron-rich structures (Eq. (6)). The microscale contribution is therefore very sensitive to the cellular
113 distribution of iron. Depending on the theoretical regime, the microscale relaxation rates can
114 be determined from the Larmor frequency perturbation induced by iron (Eq. (6)) or the spatial
115 two-point correlator of the latter (Eqs. (8), (9)). In the specific case of sparse iron-rich cells, R_2^* is a
116 highly informative biomarker: It is proportional to the susceptibility difference between the cells
117 and their surrounding (Eq. (7)) (*Yablonskiy and Haacke, 1994*).

118 Importantly, iron stored in ferritin and neuromelanin contributes differently to relaxation rates
119 both for nanoscale and microscale relaxation mechanisms, since these two iron binding forms differ
120 with respect to their magnetic properties and accessibility to water (*Gossuin et al., 2000; Trujillo*
121 *et al., 2017; Brooks et al., 1998; Cho et al., 2004; Schäfer-Nolte, 2014; Zecca et al., 2004a*).

122 To summarize, iron-induced R_2^* and R_2 are driven by several mechanisms, dependent on different
123 aspects of the cellular iron distribution. Estimating the dominating relaxation mechanism in the
124 nigrosomes and quantifying the contribution of DN to R_2^* and R_2 requires comprehensive knowledge
125 of the quantitative 3D microscopic iron distribution in both chemical forms.

126 Results

127 Enhanced R_2^* in the nigrosomes is induced by iron

128 In this section, we show that iron is the main contributor to effective transverse relaxation in the
129 nigrosomes by (i) a qualitative comparison between MRI contrast in *post mortem* SN tissue and
130 histology and (ii) a quantitative analysis of the iron-induced contribution to R_2^* and R_2 in a tissue
131 iron extraction experiment.

132 To examine the origin of effective transverse relaxation in the nigrosomes qualitatively, we
133 compared quantitative MRI acquired at 7 T to histology and quantitative iron mapping on three
134 tissue blocks containing SN (sample 1: Figs. 1, 2; samples 2 and 3: Fig. S1). High resolution R_2^* and R_2
135 maps, ultra-high resolution T_2^* -WI, and histology were precisely registered using vascular landmarks
136 (marked with asterisks for sample 1 in Fig. 1B, C). In sample 1, the nigrosomes N1 and N3 were
137 identified on histological sections as areas with high density of neuromelanin-rich dopaminergic
138 neurons (Fig. 1C), low calbindin staining intensity (Fig. S1G1), and with morphology according to

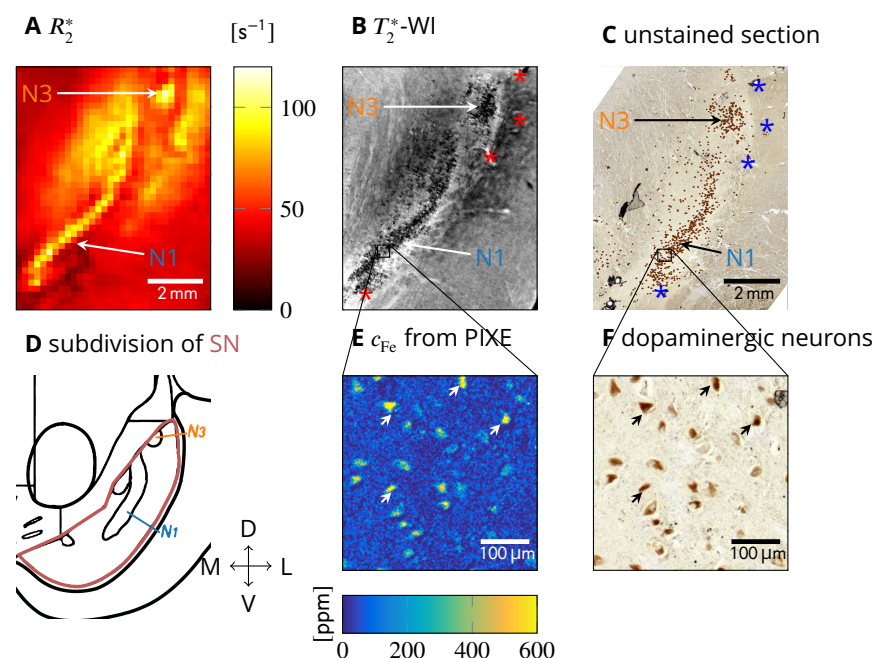


Figure 1. Quantitative histology and MRI (sample 1 shown, results for samples 2 and 3 are presented in Fig. S1). A: On a quantitative R_2^* map of SN, nigrosomes N1 and N3 are visible as hyperintense areas. B: On ultra-high resolution T_2^* -WI of SN, granular hypointensities are visible in N1 and N3. C: An unstained tissue section including SN shows N1 and N3 as areas with increased density of neuromelanin-positive (brown) DN (DN marked with a brown dot for better visibility). The vascular landmarks used for co-registration of MRI and histology are marked with asterisks in B and in C. D: Subdivision of SN along medial (M), lateral (L), ventral (V), and dorsal (D) directions, showing an elongated N1 and a circular N3 (adapted from (Damier *et al.*, 1999b)). E: Quantitative iron map from a region in N1 obtained with PIXE. An increased iron concentration was observed in cytoplasm of neuromelanin-positive DN. F: Enlargement of the region of interest (ROI) within N1 marked in C, on which the PIXE measurement (E) was done. Brown neuromelanin domains in DN were identified. Examples of identified DN are marked with arrows in E and in F.

139 the anatomical subdivision of SN (Damier *et al.*, 1999b): an elongated, curved N1 located ventro-
 140 medially and a circular N3 located dorso-laterally (Fig. 1C, D). Nigrosomes appeared hyperintense
 141 on quantitative R_2^* maps of all tissue samples, showing high contrast to surrounding SN tissue (Figs.
 142 1A, 2B, S1B1-3). On ultra-high resolution T_2^* -WI of all three samples, granular hypointensities were
 143 visible at the location of the nigrosomes, pointing towards the presence of magnetic field perturbers
 144 with size smaller than and distance larger than $50\ \mu\text{m}$, which was the approximate length of the
 145 voxel edge in the T_2^* -WI acquisition (e.g., Fig. 1B). Quantitative iron maps obtained with PIXE on all
 146 three samples revealed microscopic spots of increased iron concentration in the nigral areas of
 147 enhanced R_2^* (Figs. 1E; S2A, C). These hot spots were identified as neuromelanin-rich domains within
 148 DN in all samples (Figs. 1F; S2B, D). Combining this finding with MRI results, we hypothesize that DN
 149 containing iron-rich neuromelanin are the microscopic magnetic perturbers causing increased R_2^* in
 150 the nigrosomes.

151 To test the above hypothesis and quantify the iron-induced R_2^* and R_2 in the nigrosomes, we
 152 analyzed quantitative MRI data acquired before and after chemical tissue iron extraction on sample
 153 1 (Fig. 2, Table 1). Before iron extraction, strong R_2^* contrast was observed between the nigrosomes
 154 and the surrounding tissue (S), with significantly higher R_2^* values in the nigrosomes (Fig. 2B, D). No
 155 contrast between the nigrosomes and the surrounding tissue was observed in R_2 maps (Fig. 2C, D).
 156 R_2 values were much smaller than R_2^* values.

157 Iron extraction strongly reduced the R_2^* values in the nigrosomes (Table 1). The contrast between
 158 the nigrosomes and the surrounding tissue disappeared (Fig. 2B, D) and no granular T_2^* -WI hy-
 159 pointensities in nigrosomes were visible anymore (Fig. 2A). R_2 relaxation rates were slightly reduced

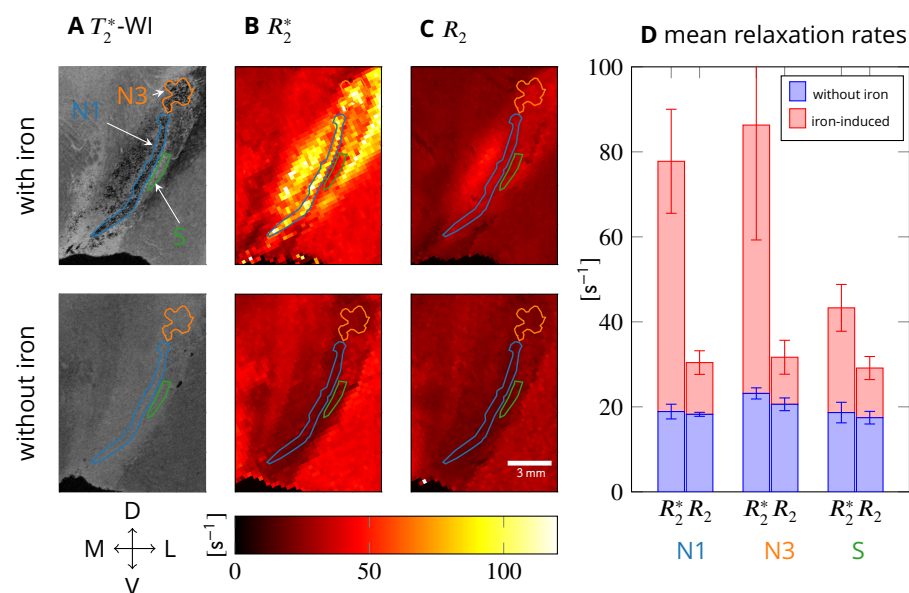


Figure 2. Transverse and effective transverse relaxation before (top row) and after chemical iron extraction (bottom, sample 1). A: Granular hypointensities in N1 and N3 disappeared after iron removal on 50 μm resolution T_2^* -WI. B: On quantitative R_2^* maps, the contrast between N1, N3, and the surrounding tissue (ROI S) was lost after iron extraction. C: On quantitative R_2 maps, no contrast between N1, N3, and S was observed before and after iron extraction. D: R_2^* and R_2 averaged over ROIs N1, N3, and S before iron extraction (red plus blue bar) and after (blue bar) are shown. The difference in relaxation rates before and after iron extraction (red bar) is hence the iron-induced relaxation rate. Iron induced five times more R_2^* than R_2 in N1 and N3, in S two times more R_2^* than R_2 . After iron extraction, R_2^* and R_2 were almost equal in N1, N3, and S. The error bars indicate the standard deviation in the ROI. Anatomical directions are indicated as in Fig. 1.

160 after iron extraction in N1, N3, and S (Table 1; Fig. 2C, D). No difference between averaged R_2^* and
 161 R_2 was found in the nigrosomes after tissue iron extraction (Fig. 2D). In N1 and N3, the iron-induced
 162 contribution to R_2^* , estimated as a difference in relaxation rates before and after iron extraction,
 163 was almost 5 times higher than the iron-induced R_2 contribution. This observation points towards
 164 static dephasing as the dominating iron-induced relaxation mechanism.

165 **DN somata have the highest iron concentration, but most of the nigral iron is lo-**
 166 **cated in ferritin outside of the DN's somata**

167 In this section, we quantify the 3D microscopic iron distribution in nigrosome N1 using a combination
 168 of classical histology and PIXE. The 3D microscopic iron maps were used to (i) determine the
 169 distribution of iron between dopaminergic neurons and other tissue components in N1 and (ii) to
 170 inform our biophysical model of iron-induced MRI contrast.

171 Quantitative cellular iron concentration maps in the nigrosomes were obtained using PIXE

Table 1. Relaxation rates R_2 and R_2^* before and after tissue iron extraction averaged over ROIs in nigrosomes N1 and N3 and surrounding tissue S (see Fig. 2A for region definitions). The error is given as the standard deviation in the ROI.

ROI	before iron extraction		after iron extraction		iron-induced		
	R_2^* [s^{-1}]	R_2 [s^{-1}]	R_2^* [s^{-1}]	R_2 [s^{-1}]	R_2^* [s^{-1}]	R_2 [s^{-1}]	$R_2^* - R_2$ [s^{-1}]
N1	77.8 ± 12.1	30.4 ± 2.4	18.9 ± 1.7	18.2 ± 1.5	58.9 ± 12.2	12.2 ± 2.8	46.7 ± 12.5
N3	86.3 ± 27.0	31.7 ± 3.8	23.2 ± 1.3	20.6 ± 1.4	63.1 ± 27.0	11.1 ± 4.0	52.0 ± 27.3
S	43.3 ± 5.0	29.1 ± 2.3	18.7 ± 2.5	17.4 ± 1.5	24.6 ± 5.6	11.7 ± 2.8	12.9 ± 6.3

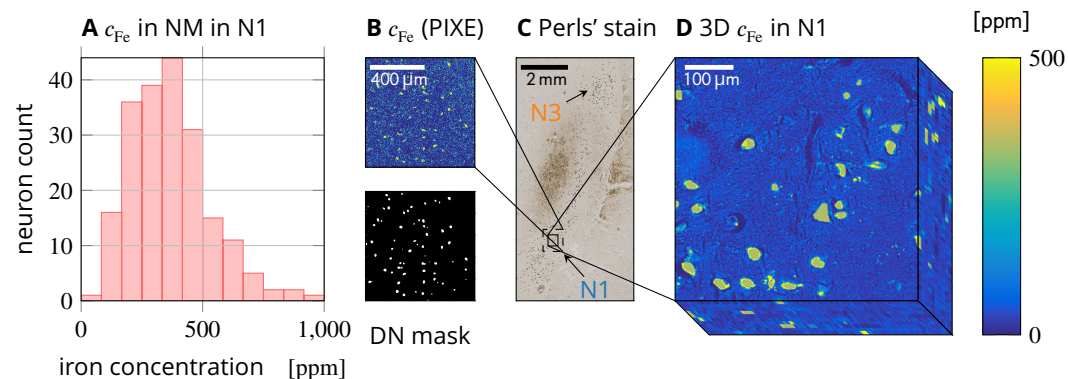


Figure 3. Quantitative iron histology of N1 in sample 1. A: Histogram of local iron concentrations found in neuromelanin (NM) domains in N1. B: Quantitative iron concentration maps obtained with PIXE on an unstained section (top) were masked using neuromelanin maps (bottom) to obtain the local concentration of iron bound to ferritin and neuromelanin (other PIXE measurement areas indicated in Fig. S1D1). C: N1 is visible as a stripe of high DN density on a section stained with Perls' solution for iron. D: A 3D quantitative iron map of N1 was generated by calibrating and co-registering 10 adjacent sections stained with Perls' solution for iron. This volume was used for biophysical modeling.

Table 2. Local iron concentration associated with neuromelanin (NM) and ferritin (FT) averaged over PIXE measurement areas in different samples. The concentration error is given as the standard error of mean (SEM) in the masked region in the PIXE iron maps. The error of the NM volume fraction is given as SEM over PIXE measurement areas for the first sample, on which PIXE was done on several ROIs.

sample	$c_{\text{Fe,NM}}$ [ppm]	$c_{\text{Fe,FT}}$ [ppm]	NM volume fraction	NM iron fraction	$R_{2,\text{micro,DN}}^*$ (Eq. (7)) [s^{-1}]
1	387 ± 5	56 ± 3	$(1.97 \pm 0.06) \%$	$(12.2 \pm 0.6) \%$	23.5 ± 0.4
2	671 ± 11	184.0 ± 0.8	3.5 %	$(11.8 \pm 0.2) \%$	51.7 ± 1.0
3	1356 ± 11	451 ± 3	13.5 %	$(32.0 \pm 0.3) \%$	390.0 ± 3.4

172 (sample 1: Fig. 3; samples 2 and 3: Figs. S2, S3). The local concentration of iron bound in two
173 chemical forms was determined from these maps, assuming that iron within DN is mainly bound in
174 neuromelanin and outside of DN mainly in ferritin (Table 2). Histograms of local iron concentrations
175 in neuromelanin in N1 were generated by using masks of the neuromelanin in the DN's somata
176 (sample 1: Fig. 3A, other samples: Fig. S3; Fig. 3B).

177 In sample 1, a strongly increased local iron concentration ((387 ± 5) ppm) was found in the
178 neuromelanin within the DN's somata, while a significantly lower local concentration ((56 ± 3) ppm) of
179 ferritin-bound iron was observed in the surrounding tissue. Neuromelanin occupied (1.97 ± 0.06) %
180 of the volume, containing (12.2 ± 0.6) % of all iron. While the local iron concentration in neuromelanin
181 within DN is seven times higher than in the surrounding tissue, the average tissue iron content
182 associated to neuromelanin is five times lower than that attributed to ferritin. In samples 2 and 3,
183 the results were qualitatively similar: an increased iron concentration in DN, but the majority of iron
184 bound to ferritin outside of DN (Fig. S2, Table 2). A strong variation of local iron concentration in DN
185 was found between neurons in each sample as well as between samples (Fig. S3): For sample 1, a
186 mean and standard deviation across DN of (365 ± 161) ppm was found, for sample 2 (811 ± 366) ppm,
187 for sample 3 (1495 ± 499) ppm.¹

188 For sample 1, a quantitative 3D microscopic iron concentration map of N1 was generated (Fig.
189 3D). The 3D map, spanning over several MRI voxels within N1, was obtained from co-registration of
190 ten adjacent sections stained with Perls' solution for iron. This 3D map of N1 was made quantitative
191 by calibrating the underlying Perls' stains with local iron concentration in neuromelanin and ferritin
192 from PIXE data on sample 1 (Table 2, Fig. 3B, C, D).

193 The average tissue iron content in both neuromelanin and ferritin, necessary for predicting
194 nanoscale relaxation rates, was estimated from the 3D iron concentration map. The average tissue
195 iron content in neuromelanin was $\bar{c}_{\text{Fe,NM}} = (8.9 \pm 0.2)$ ppm.² Outside of the DN somata masks, the
196 average tissue iron content in ferritin was $\bar{c}_{\text{Fe,FT}} = (51.1 \pm 3.0)$ ppm.³

197 **Microscopic iron distribution causes most of iron-induced R_2^* , which is accurately** 198 **described by the static dephasing approximation**

199 At this point, we have determined all necessary parameters for the biophysical model and proceed
200 with estimating iron-induced relaxation rates originating from nanoscale and microscale processes.
201 We identify the dominating contribution and appropriate theoretical description by comparing
202 theoretical predictions with experimental data obtained before and after tissue iron extraction.

203 **Molecular interactions on the nanoscale**

204 The nanoscale contributions of neuromelanin- and ferritin-bound iron were estimated to be
205 $R_{2,\text{nano,NM}} = (7.54 \pm 0.11) s^{-1}$ and $R_{2,\text{nano,FT}} = (1.14 \pm 0.07) s^{-1}$, respectively. We estimated them using Eq.
206 (3) and the average tissue iron content in neuromelanin and ferritin obtained above. Interestingly,
207 despite the fact that most of the iron is bound in ferritin, neuromelanin-bound iron in DN contributes
208 dominantly to nanoscale relaxation due to its higher relaxivity. The total predicted nanoscale con-
209 tribution $R_{2,\text{nano}}^* = R_{2,\text{nano}} = (8.67 \pm 0.13) s^{-1}$ is much lower than the iron-induced R_2^* ($(42 \pm 11) s^{-1}$), but
210 comparable with iron-induced R_2 ($(11.3 \pm 1.8) s^{-1}$) in this volume.⁴ Hence, the nanoscale relaxation
211 is not the dominant relaxation mechanism for R_2^* , but may explain the observed iron-induced R_2 .

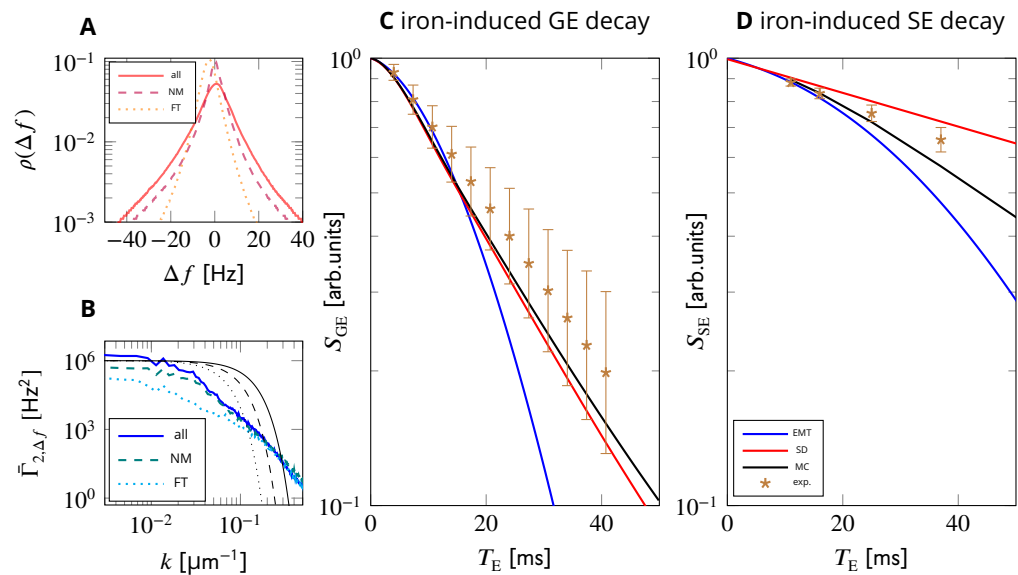


Figure 4. Modeling iron-induced microscale relaxation in N1 for sample 1. A: Larmor frequency shift histograms for all iron (solid), iron in neuromelanin (NM, dashed) and iron in ferritin (FT, dotted) show that iron in neuromelanin contributes most of the spectral width, which causes static dephasing (SD) decay. B: In effective medium theory (EMT), Larmor frequency two-point correlators are low-pass filtered to account for diffusion. Example diffusion kernels are shown in solid/dashed/dotted black for echo times $T_E = 10/20/40$ ms. C: GE signal decay predicted using SD is in good agreement with Monte Carlo simulations (MC) and experimental data, while EMT underestimates the signal for echo times longer than 20 ms. D: SE signal decay predicted with EMT shows faster relaxation than the decay from the MC simulation. Both MC and EMT somewhat overestimate the experimental SE decay. The predicted nanoscale relaxation rates were added to the shown iron-induced signal decays in C and D. The experimental data shown in C and D are experimentally derived iron-induced decays, calculated by subtracting the non-iron-induced relaxation rates in N1 obtained from the iron extraction experiment. The error bars indicate the SEM of experimental relaxation rates.

212 Heterogeneous cellular iron distribution on the microscale
213 Contributions of the microscopic heterogeneous cellular iron distribution to R_2^* and R_2 were esti-
214 mated using Monte Carlo simulations and two analytic approximations to the MRI signal: static
215 dephasing and motional narrowing (Fig. 4). In all three approaches, the iron-induced Larmor
216 frequency shift (Fig. S4) obtained from the 3D quantitative iron map (Fig. 3D) was used.

217 A Monte Carlo simulation of water diffusion within this 3D Larmor frequency shift map predicted
218 iron-induced GE and SE signal decays according to Eqs. (4) and (5).

219 For the static dephasing approximation, the iron-induced R_2^* was calculated from the histogram
220 of the intravoxel iron-induced Larmor frequency perturbation (Fig. 4A). This histogram was numeri-
221 cally Fourier transformed to obtain the iron-induced GE signal decay (Fig. 4C, Eq. (6)).

222 For the motional narrowing approximation, an effective medium theory was used (Eqs. (8), (9)).
223 Herein, the two-point correlator of the iron-induced Larmor frequency perturbation was convolved
224 with a diffusion kernel (Fig. 4B).

225 The predictions of Monte Carlo simulations were in agreement with the experimental data for R_2^*
226 and slightly overestimated R_2 .⁵ For the comparison, the predicted nanoscale relaxation rates were
227 added to the microscale decay, while the non-iron-induced relaxation rate from the iron extraction
228 experiments was subtracted from the experimental relaxation rate. The excellent agreement for R_2^*
229 indicates that our model captures iron-induced effective transverse relaxation accurately.

230 The static dephasing approximation agrees very well with Monte Carlo simulations of the GE
231 decay and the experimental R_2^* . The prediction of the effective medium theory only agrees with the
232 Monte Carlo simulation and the experiment for echo times T_E less than 20 ms, but overestimates GE
233 and SE decay rates for larger echo times.⁶ From the good match of the static dephasing model and
234 poor match of the effective medium theory model we can conclude that static dephasing is the
235 relaxation regime of the largest part of effective transverse relaxation in N1.

236 DN are the main cellular source of iron-induced R_2^* in N1

237 In this section, we use the developed biophysical model to estimate the contribution of dopaminer-
238 gic neurons to effective transverse relaxation rates in the nigrosomes in order to assess the sensitivity
239 and specificity of R_2^* to this cell type.

240 The total R_2^* and R_2 relaxation rates in N1 were estimated by adding the iron-induced relaxation
241 rates from nano- and microscale mechanisms to the non-iron induced relaxation rates averaged
242 over N1 from the iron extraction experiment (Fig. 5). Predicted relaxation rates agreed well with
243 experimental values: For R_2^* , the sum of the predicted iron-induced R_2^* and measured non-iron-
244 induced R_2^* in N1, $(68.4 \pm 1.8) \text{ s}^{-1}$, was within the standard error of mean of the experimental R_2^* of
245 $(61 \pm 11) \text{ s}^{-1}$. For R_2 , the sum of the predicted iron-induced R_2 and measured non-iron-induced R_2
246 was $(37.1 \pm 1.6) \text{ s}^{-1}$, somewhat overestimating the experimentally determined R_2 of $(29.6 \pm 0.9) \text{ s}^{-1}$.

247 According to our simulations, R_2^* is the parameter most sensitive to iron in DN somata. The
248 microscale contribution from only the neuromelanin-bound iron in DN of $R_2^* = (22.32 \pm 0.15) \text{ s}^{-1}$ was
249 predicted using a Monte Carlo simulation. This value agrees well with the analytic prediction of
250 effective transverse relaxation resulting from spherical iron-rich cells in static dephasing (Eq. (7)) of
251 $R_2^* = (20.6 \pm 0.4) \text{ s}^{-1}$. Hence, the R_2^* induced by iron in DN somata is proportional to susceptibility

¹These mean values are different from the values reported in Table 2, because here each DN was weighted equally, while in the mean values in Table 2 the iron concentration is weighted with the DN's area in the microscopy section.

²Throughout this paper, the unit ppm is used as $\mu\text{g g}^{-1}$ wet tissue weight.

³These average tissue iron contents differ slightly from the values reported for the PIXE measurements (Table 2), because the averages were taken over different ROIs (Figs. 3C, S1D1).

⁴The experimental values were calculated as the difference between the measured relaxation rates in the MRI voxels corresponding to the 3D quantitative iron map and the non-iron-induced relaxation rates averaged over N1 from the iron extraction experiment, which was performed on the contralateral side of the same sample.

⁵The error of the predicted relaxation rates was estimated from the residuals of the linear fit, as this was far larger than the error of the used average tissue iron contents (Table 2).

⁶This is not unexpected, as the parameter α , which determines the applicability of the effective medium theory (Kiselev and Novikov, 2018), is larger than one for $T_E = 20 \text{ ms}$. We estimated the parameter $\alpha = 2\pi\sqrt{\langle\Delta f^2\rangle}T_E \approx 1.9$, using the standard deviation of the Larmor frequency $\sqrt{\langle\Delta f^2\rangle} = 14.7 \text{ s}^{-1}$.

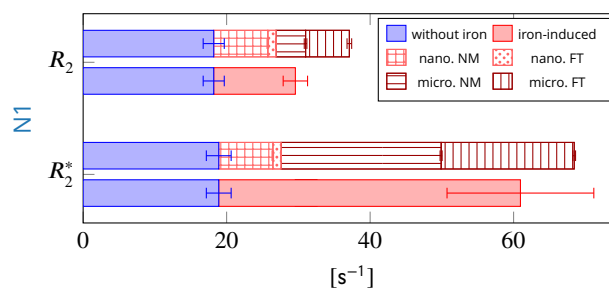


Figure 5. Comparison of predictions (patterned) to experimental transverse relaxation rates (solid color). The iron-induced relaxation rates (red) were obtained by subtracting the non-iron-induced relaxation rates in N1 from the iron extraction experiment (blue) from the relaxation rates measured in the volume corresponding to the 3D iron map. Top: The sum of the predicted nano- and microscale R_2 in N1 somewhat overestimates the iron-induced R_2 . Neuromelanin- (NM) and ferritin-bound (FT) iron contributes equally to the microscale R_2 relaxation rate, while neuromelanin dominates the nanoscale relaxation rates. Bottom: In N1, the sum of the predictions is in agreement with the experimental iron-induced R_2^* within the SEM indicated by the error bar. The contribution of neuromelanin-bound iron to microscale R_2^* (micro. NM, horizontal stripes) dominates. The contribution of ferritin-bound iron to microscale R_2^* was estimated by subtracting the R_2^* from neuromelanin-bound iron from the R_2^* predicted for all iron.

252 difference between DN and the surrounding tissue (Eq. (7)). In case of iron-rich DN in N1, the
 253 susceptibility difference is predominantly contributed by neuromelanin-bound iron: Neurome-
 254 lanin's susceptibility per iron load is almost three times higher than ferritin's and the local iron
 255 concentration in neuromelanin is more than six times higher. Thus, the R_2^* contribution from DN
 256 is a linear function of their average tissue iron content, i.e. the product of the average iron load
 257 of DN and the neuronal density. Adding the nanoscale contribution of neuromelanin-bound iron,
 258 iron in DN caused $(43.6 \pm 0.6)\%$ of the total R_2^* and $(60.2 \pm 1.2)\%$ of the iron-induced R_2^* . R_2 was
 259 less sensitive to iron in DN, which caused $(31.4 \pm 1.8)\%$ of the total R_2 and $(61.70 \pm 1.53)\%$ of the
 260 iron-induced R_2 .

261 Interestingly, iron-induced R_2^* and R_2 are two times more affected by neuromelanin-bound iron
 262 than the iron-induced bulk susceptibility: Iron in DN's neuromelanin contributes merely $(29.3 \pm 0.4)\%$
 263 to the iron-induced bulk susceptibility, as calculated by dividing the product of the DN's volume
 264 fraction of 2.6% and their average susceptibility of (1111 ± 15) ppb by the average susceptibility in
 265 the volume of the 3D quantitative iron map of (99 ± 5) ppb.

266 Nigrosome integrity can be assessed with MRI *in vivo*

267 In this section, we examine theoretically how high the contribution of DN to R_2^* in N1 would be in *in vivo*
 268 MRI and whether nigral iron quantification could be achieved in reasonable scan time. To this
 269 end, we extrapolated our finding from *post mortem* tissue to the *in vivo* MRI case by accounting for
 270 differences in temperature and tissue diffusion properties.

271 The body temperature *in vivo* as compared to room temperature in our *post mortem* experiments
 272 leads to a decreased iron-induced relaxation rate due to the temperature-induced decrease of
 273 iron's magnetic susceptibility. Since the static dephasing contribution described by Eq. (6) scales
 274 linearly with magnetic susceptibility, and the susceptibility of iron is inversely proportional to the
 275 temperature, we expect a 5% decrease of the iron-induced microscale R_2^* *in vivo*.⁷

276 Additionally, the higher diffusivity *in vivo* shifts the microscale relaxation regime in the direction
 277 of motional narrowing. While this effect may decrease the relaxation contribution of iron, making R_2^*
 278 less sensitive to this contribution, our model predicts that the microscale relaxation regime *in vivo* is
 279 still close to static dephasing (Fig. S5): a Monte Carlo simulation predicted $R_2^* = (37.7 \pm 0.3) s^{-1}$, while
 280 the prediction for static dephasing was $R_2^* = (40.70 \pm 0.06) s^{-1}$. The combined effect of decreased
 281 susceptibility and faster diffusion was 7.8% less R_2^* *in vivo*, which was estimated using Monte Carlo

⁷This was estimated using Curie's law: $\chi_{in vivo} / \chi_{post mortem} = T_{post mortem} / T_{in vivo} = 293 K / 310 K \approx 95\%$.

282 simulation (Fig. S5). Importantly, thus our model predicts that also *in vivo* R_2^* is a parameter sensitive
283 to the average tissue iron content in DN.

284 The nanoscale R_2 induced by ferritin-bound iron was reported to decrease by 15 % due to a
285 temperature increase from room to body temperature (Gossuin et al., 2000). For neuromelanin-
286 bound iron, no such data was published, but a similar decrease in nanoscale R_2 is expected.

287 Based on these results, we propose two potential MRI-based biomarkers for iron in the somata
288 of dopaminergic neurons. The first is the reversible part of the effective transverse relaxation rate
289 in N1 ($R_2^* - R_2$). According to our results, this parameter is completely driven by iron and on the
290 order of 50 s^{-1} (Table 1), of which about 60 % are contributed by iron in DN. We expect an even higher
291 specificity for the second biomarker, the difference in R_2^* between N1 and the directly surrounding
292 tissue (e.g. area S in Fig. 2). This parameter is analytically linked to the average tissue iron content
293 in DN as shown above, if the contribution of ferritin-bound iron is comparable in both regions.

294 While the increased temperature and diffusion constant *in vivo* decrease iron's contribution
295 to R_2^* slightly, assessing the average tissue iron content of dopaminergic neurons is in reach of *in*
296 *vivo* MRI relaxometry. Strong contrast in R_2^* was observed between the millimeter-thin N1 and the
297 surrounding tissue with more than 40 % increase in R_2^* in the DN-rich area. Hence, *in vivo* nigrosome
298 characterisation with 7T MRI requires quantitative maps of R_2^* and R_2 with sub-millimeter resolution
299 and signal-to-noise ratio (SNR) of at least 4 to achieve a contrast-to-noise ratio of 2. A multi-echo
300 GE acquisition with a resolution of $500 \mu\text{m}$ resulting in R_2^* maps with averaged SNR of about 20
301 was demonstrated at 7T *in vivo* (Tardif et al., 2016), opening the path for *in vivo* assessment of
302 substantia nigra's substructure.

303 Discussion

304 This work establishes a comprehensive biophysical model of iron-induced transverse and effective
305 transverse relaxation rates in the nigrosomes in human *substantia nigra*. We demonstrated that
306 iron in neuromelanin-rich dopaminergic neurons in the nigrosomes is the predominant contrast
307 driver (Figs. 1, 2). Using quantitative cellular iron maps and biophysical modeling, we predicted
308 iron-induced relaxation rates from first principles and quantified the impact of different relaxation
309 mechanisms induced by iron stored in two chemical forms. We characterized the distribution of iron
310 in these two forms, ferritin and neuromelanin (Figs. 3, S3), and separately estimated their impact
311 on quantitative MRI parameters. In nigrosome N1, we found most of the iron bound in ferritin and
312 only about 11.8 % to 32.0 % stored in neuromelanin in DN (Table 2). Despite its lower concentration,
313 neuromelanin-bound iron was the major contributor to nigral R_2^* relaxation, explaining 60 % of iron-
314 induced relaxation rates in a representative volume of several MRI voxels within N1 (Fig. 5). Both
315 quantitative biophysical modeling and qualitative assessment indicated that the heterogeneous
316 cellular iron distribution on the microscale is the main effective transverse relaxation mechanism in
317 N1. This contribution is well described by the static dephasing approximation (Fig. 4).

318 Biophysical modeling informs the design of MRI-based biomarkers of nigrosome 319 integrity

320 Our results provide important guidance for the interpretation and development of MRI-based
321 biomarkers of nigrosome integrity *in vivo*. We proposed two potential biomarkers of iron in DN:
322 The reversible part of the iron-induced effective transverse relaxation rate ($R_2^* - R_2$) in N1 and the
323 difference in R_2^* between N1 and the directly surrounding DN-poor tissue. Both parameters are
324 driven by the average tissue iron content of neuromelanin clusters, i.e. the product of local iron
325 concentration in DN and their density (Yablonskiy and Haacke, 1994). We expect this relation to
326 hold *in vivo*, as the predicted iron-induced relaxation rates were reduced by merely 7 % due to
327 temperature and tissue fixation effects (Fig. S5). These potential biomarkers of the averaged tissue
328 iron content in DN are likely informative because the density of DN and their iron load strongly
329 varies across the SN and also between individuals (Figs. S1, S3). Thus, they are expected to be

330 sensitive to age-related iron accumulation in DN (*Zecca et al., 2004a*) and to DN depletion (*Damier*
331 *et al., 1999b*) and therefore potentially to cognitive and motor impairment in PD (*Tambasco et al.,*
332 *2019*).

333 We estimated that a biomarker of iron in DN is in reach of state-of-the-art MRI methods (*Tardif*
334 *et al., 2016*). Recently developed methods for prospective motion correction and physiological
335 noise correction (*Vannesjo et al., 2015; Versluis et al., 2010; Stucht et al., 2015*) promise to improve
336 data quality even further (*Trampel et al., 2019; Lüsebrink et al., 2017; Metere et al., 2017*).

337 Our generative biophysical model has fundamental implications for the understanding of
338 relaxation mechanisms in the human brain: It demonstrates that knowledge about the cellular
339 iron distribution and iron's chemical form are indispensable for interpreting GE and SE signal
340 decays. Current models of iron-induced MRI parameters (*Haacke et al., 2005; Stüber et al., 2014;*
341 *Langkammer et al., 2012; Yao et al., 2009*) often oversimplify the impact of tissue iron by using
342 a single empirical proportionality coefficient between the average tissue iron concentration and
343 the MRI parameter across brain areas. For areas with similar average tissue iron concentrations,
344 as the motor cortex with 50 ppm (*Hallgren and Sourander, 1958*) and N1 in sample 1 with 60 ppm
345 (Fig. 3), one such model for R_2^* (*Stüber et al., 2014*) predicts $R_2^* = 15.6 \text{ s}^{-1}$ in the motor cortex and
346 $R_2^* = 17.7 \text{ s}^{-1}$ in N1. The model predicts relaxation rates accurately in the motor cortex, where we
347 estimate an approximate iron-induced $R_2^* \approx 15 \text{ s}^{-1}$.⁸ In N1, however, the model explains less than
348 half of the iron-induced $R_2^* = (42 \pm 11) \text{ s}^{-1}$.⁹ Our model is able to explain this difference by taking
349 iron's heterogeneous cellular distribution and its chemical form into account, predicting a total
350 iron-induced $R_2^* = (49.5 \pm 0.3) \text{ s}^{-1}$. This stresses the importance of precise and specific models as
351 presented here.

352 Our model predicts that the MRI parameters R_2^* , R_2 , and the bulk susceptibility measured with
353 QSM are all affected differently by neuromelanin- and ferritin-bound iron pools. For instance, iron
354 in DN contributes 60 % of iron-induced R_2^* , but merely 29 % of iron-induced bulk susceptibility. There-
355 fore, combining the information from all three parameters may enable the separate quantification
356 of both iron pools using the quantitative links established by our model.

357 Our approach can be extended to studies of other iron-containing structures in the human brain.
358 While there was extensive work on explaining myelin's contribution to transverse relaxation from
359 first principles (*Wharton and Bowtell, 2012*), so far only few studies addressed the microscopic
360 mechanisms of iron's contribution to R_2^* in brain structure (*Troprès et al., 2001; Wen et al., 2018*).
361 Particularly, the contributions to R_2^* of iron-rich glial cells in healthy grey and white matter, such
362 as oligodendrocytes, micro-, and astroglia, as well as iron in myelin sheaths, have not yet been
363 systematically explored. Iron is known to be accumulated in amyloid plaques and neurofibrillary
364 tangles in Alzheimer's disease (*Meadowcroft et al., 2015*) and in multiple sclerosis lesions (*Craelius*
365 *et al., 1982*). Understanding mechanisms of iron-induced relaxation in these pathologies is expected
366 to facilitate more specific disease biomarkers with diagnostic value.

367 **Our results in context of previous work**

368 The iron concentrations obtained in our study agree well with previous reports. To our knowledge,
369 only two studies reported local iron concentrations in dopaminergic neurons. In a single DN
370 in SN, the local iron concentration was 230 ppm (*Morawski et al., 2005*), while in a more recent
371 study we reported a range of local iron concentrations in DN in nigrosome N1 from 85 ppm to
372 1371 ppm¹⁰ (*Weigelt, 2019*). Both agree with the range of local iron concentrations in DN from our
373 study (Figs. 3A, S3). The sum of averaged tissue iron contents in neuromelanin and ferritin in
374 N1 (in sample 1, 2, and 3 (63.0 ± 2.5) ppm, (201.1 ± 1.2) ppm, and (573 ± 4) ppm, respectively) is on the

⁸This was estimated by subtracting from a reported $R_2^* = 31.6 \text{ s}^{-1}$ in the motor cortex (*Deistung et al., 2013*) a post-iron extraction R_2^* of 15 s^{-1} in the visual cortex (*Fukunaga et al., 2010*), as no data from the motor cortex was available.

⁹This was estimated as the difference between R_2^* measured in this area (Fig. 5) and the average R_2^* rate in N1 after iron extraction (Fig. 2D, Table 1).

¹⁰To ensure comparability, we applied the same tissue shrinkage correction as for our PIXE measurements to the reported value, which was a factor of 0.76.

375 order of the reported iron concentrations averaged across the entire SN, 48 ppm to 204 ppm (*Dexter*
376 *et al., 1989, 1991; Galazka-Friedman et al., 1996; Hallgren and Sourander, 1958; Loeffler et al.,*
377 *2002; Riederer et al., 1989; Morawski et al., 2005; Zecca et al., 2004a; Weigelt, 2019*).

378 Increased R_2^* relaxation rates in the nigrosomes are in line with recent studies (*Lee et al., 2016,*
379 *2018*). A R_2^* of $(82 \pm 25) \text{ s}^{-1}$ was observed in the nigrosomes in the first sample of our study (Fig. 2D),
380 which corresponded well to a reported R_2^* of $(103 \pm 3) \text{ s}^{-1}$ in neuromelanin-rich regions within SN in
381 *post mortem* tissue. In all examined samples, we identified the neuromelanin-rich nigrosomes as
382 regions with increased R_2^* by precisely registering R_2^* maps to histology using ultra-high resolution
383 T_2^* -WI (Figs. 1A, B, C; S1A, B, D). The R_2^* relaxation rates in samples 2 and 3 are higher than in sample
384 1, which can be attributed to the intersubject variability of local iron concentrations in and volume
385 fraction of DN's neuromelanin (Table 2, Fig. S3).

386 Our results deviate from the study by Blazejewska *et al.* (*Blazejewska et al., 2013*), who in-
387 terpreted a hyperintense feature on *post mortem* T_2^* -WI, the swallow tail, as N1. This interpreta-
388 tion was adopted in several subsequent studies (*Schwarz et al., 2014, 2018; Lehericy et al., 2014;*
389 *Mahlknecht et al., 2017*). A potential cause of this seeming contradiction may be a difference in
390 co-registration strategies or definition of nigrosomes in the two studies. In our study, ultra-high
391 resolution MRI was used for local co-registration with histology, enabling registration with a pre-
392 cision of about $100 \mu\text{m}$, while an affine co-registration of large sections was used in the earlier
393 study, potentially causing a local mismatch. In addition, Blazejewska *et al.* defined nigrosomes on
394 histological sections as areas with low calbindin immunoreactivity, while we defined nigrosomes as
395 areas with high density of dopaminergic neurons. Although we also found low calbindin immunore-
396 activity staining intensity in areas of high DN density in all samples (Fig. S1G), they did not always
397 perfectly co-align, since calbindin-poor areas were larger than areas of high DN density. On the
398 other hand, it was difficult to identify the swallow tail feature in our data, since we used tissue blocks
399 that did not always encompass the entire SN. It was recently reported that the swallow tail shows
400 intersubject variability in *in vivo* MRI data (*Cheng et al., 2019*). A further study is required to identify
401 the histological underpinning of the swallow tail feature and its exact relation to N1, including
402 precisely co-registered quantitative MRI and histology on whole brains. Such a study would be of
403 high importance for the development of an *in vivo* nigral biomarker, since the *substantia nigra* is a
404 heterogeneous structure, containing not only the nigrosomes but also afferent and efferent fibers.
405 As relaxation is impacted by different structures across SN, it will be crucial to look at the regions
406 where dopaminergic neurons contribute predominantly.

407 **Experimental limitations and biophysical modeling assumptions**

408 Our conclusions about relaxation mechanisms were drawn from experiments on formalin-fixed
409 *post mortem* tissue, which differ from *in vivo* tissue in several ways. The minor effects of vasculature,
410 increased temperature, and increased diffusion coefficient (*Birkl et al., 2016*) *in vivo* were already
411 discussed.

412 Additionally, our model probably underestimates iron-induced relaxation *in vivo* by 5%, as the
413 labile iron pool is washed out during preparation, before PIXE measurements and histochem-
414 istry are performed. The labile pool contains 5% of the total iron in soluble proteins such as
415 transferrin (*Kakhlon and Cabantchik, 2002; Stüber et al., 2014*).

416 Except for the labile iron pool, we assume that the cellular iron distribution observed in *post*
417 *mortem* SN tissue reflects well the *in vivo* cellular iron distribution. Post-fixation iron accumulation
418 that changed the MRI contrast was observed recently in neuromelanin-rich neurons in *post mortem*
419 locus coeruleus (*Betts et al., 2019*). However, this process is most likely specific to locus coeruleus:
420 There, the neuromelanin-containing neurons are iron-poor under physiological conditions, while
421 neuromelanin in SN is rich in iron (*Zecca et al., 2004b*).

422 In the chemical iron extraction experiment, which we used to quantify iron-induced relaxation
423 in SN, we assumed that all changes in MRI parameters are attributed to missing iron. The chemical
424 iron extraction procedure could have additional effects on the tissue and alter non-iron-induced

425 relaxation rates. Such alterations did most likely not affect R_2^* , as we found no significant differences
426 between R_2^* pre- and post-extraction in the iron-poor crus cerebri region on a quantitative R_2^* map
427 (Fig. 2B, ventro-lateral of ROI S).

428 While nanoscale processes are merely a minor driver of iron-induced R_2^* according to our anal-
429 yses, the relaxivities of iron in neuromelanin and ferritin used in the biophysical model could be
430 different from relaxivities in tissue as they were determined *in vitro* (Trujillo *et al.*, 2017; Gossuin
431 *et al.*, 2002). Particularly for neuromelanin, the difference in molecular structure and granularity of
432 the synthetic melanin used *in vitro* may affect its effective relaxivity. It is experimentally cumber-
433 some to overcome these limitations. However, as the iron extraction experiment shows that iron
434 contributes much stronger to R_2^* than to R_2 and nanoscale processes contribute equally to R_2 and
435 R_2^* , they are of minor interest here.

436 For modeling relaxation rates due to processes on the microscale, we estimated the effective
437 susceptibility per iron load of DN using Curie's law for an isolated spin 5/2, which is an oversimplifi-
438 cation in view of the two iron binding sites of neuromelanin (Zucca *et al.*, 2017). An experiment to
439 determine neuromelanin's susceptibility would be of great help to refine our model.

440 While the high correspondence between experimental results and theory makes it unlikely that
441 any major contributor was overlooked, relaxation effects due to more fine grained iron distribution
442 patterns smaller than the voxel size of the 3D iron concentration map were disregarded. The 3D
443 iron concentration maps had a resolution of 0.88 μm in plane and a slice thickness of 10 μm , which
444 could be increased using electron microscopy.

445 The model did not explicitly include myelin as a driver of R_2^* and R_2 contrast, since the myelin
446 concentration in N1 is low, as can be seen on Luxol stains for myelin (Fig. S1F1). Using the model in
447 other areas will require to enhance it and take myelin's contribution into account.

448 Importantly, the theoretical predictions were compared to experimental values in a region
449 of four MRI voxels. It was limited by the area of neuron-to-neuron registration, comprising a
450 volume of 440 $\mu\text{m} \times 440 \mu\text{m} \times 100 \mu\text{m}$. Therefore, the relative contributions of different relaxation
451 mechanisms, reported in Fig. 5, correspond to few representative voxels and were not averaged
452 across nigrosomes. To extend the theory to other regions in SN, the comparison may be performed
453 on a larger region. This would require the challenging co-registration of the entire SN by identifying
454 shared DN on sections stained with Perls' solution for iron.

455 Conclusion

456 In this paper, we develop a generative model of iron-induced transverse relaxation in nigrosome 1,
457 informed by 3D quantitative iron histology. Our biophysical model constitutes an important step on
458 the road toward a unified, quantitative understanding of iron-induced MRI relaxation in the human
459 brain. We demonstrate mechanistically that dopaminergic neurons contribute predominantly to
460 iron-induced R_2^* , although their neuromelanin only contains a minority of tissue iron. By linking R_2^*
461 to the averaged tissue iron content in dopaminergic neurons, this study lays the groundwork for
462 developing a biomarker of nigral integrity. Such a biomarker will help understanding the interplay
463 of iron accumulation and neuronal depletion in healthy ageing and Parkinson's disease, as an
464 important step toward early stage PD diagnosis.

465 Materials and Methods

466 Theory of Iron-Induced Transverse Relaxation

Iron contributes to transverse and effective transverse relaxation rates (R_2 and R_2^* , respectively)
through processes occurring at different temporal and spatial scales (Kiselev and Novikov, 2018).
These processes can be categorized into molecular interactions on the nanoscale and dephasing
due to a heterogeneous cellular iron distribution on the microscale (Kiselev and Novikov, 2018). We
assume that the contributions to R_2^* and R_2 of processes occurring on these two spatial scales are

statistically independent.¹¹ In this case, the decays of both spin and gradient echo signals (S_{GE} and S_{SE}) can be described as a product of decays induced by each process:

$$S_{GE}(T_E) = \exp\left(-\int_0^{T_E} dt R_{2,nano}^*\right) \cdot \exp\left(-\int_0^{T_E} dt R_{2,micro}^*\right) \cdot \exp\left(-R_{2,other}^* T_E\right), \quad (1)$$

$$S_{SE}(T_E) = \exp\left(-\int_0^{T_E} dt R_{2,nano}\right) \cdot \exp\left(-\int_0^{T_E} dt R_{2,micro}\right) \cdot \exp\left(-R_{2,other} T_E\right), \quad (2)$$

467 where $R_{2,nano/micro}$ and $R_{2,nano/micro}^*$ are the iron-induced transverse and effective transverse relaxation
 468 rates, respectively, resulting from processes on the nano- and microscale. They are in general
 469 time-dependent, allowing for non-exponential behaviour. $R_{2,other}$ and $R_{2,other}^*$ are the relaxation rates
 470 induced by tissue components others than iron.

471 Molecular Interactions on the Nanoscale

472 On the nanoscale, spin-spin interactions of water protons with iron electrons result in transverse
 473 MRI relaxation. Acting on the nanometer length scale, these processes depend on the iron binding
 474 site (iron spin state and water accessibility), but are independent of the cellular distribution of
 475 iron (*Kiselev and Novikov, 2018*). Since the diffusion time over the nanoscale distances is much
 476 smaller than the echo time of an MRI experiment, this relaxation mechanism results in a linear-
 477 exponential decay and contributes equally to transverse and effective transverse relaxation rates,
 478 i.e. $R_{2,nano} = R_{2,nano}^*$.

479 The contributions of ferritin- and neuromelanin-bound iron to the nanoscale transverse re-
 480 laxation rate can be described by empirical relaxivities measured in ferritin and neuromelanin
 481 solutions at room temperature, physiological pH, and a static magnetic field of 7 T used in this study:

$$R_{2,nano} = R_{2,nano}^* = r_{2,FT} \cdot \bar{c}_{Fe,FT} + r_{2,NM} \cdot \bar{c}_{Fe,NM}, \quad (3)$$

483 where $r_{2,FT} = 0.0223 \text{ s}^{-1}/\text{ppm}$ (*Gossuin et al., 2002*) and $r_{2,NM} = 0.847 \text{ s}^{-1}/\text{ppm}$ (*Trujillo et al., 2017*)
 484 are the relaxivities of iron in ferritin and neuromelanin, respectively,¹² and $\bar{c}_{Fe,FT}$ and $\bar{c}_{Fe,NM}$ are
 485 the average tissue iron contents in ferritin and neuromelanin, respectively, i.e. the local iron
 486 concentrations associated to the chemical forms ($c_{Fe,FT}$ and $c_{Fe,NM}$) multiplied with their volume
 487 fraction $1 - \zeta$ and ζ , respectively.

488 Heterogeneous Cellular Iron Distribution on the Microscale

489 The MRI signal from brain tissue is affected by dephasing due to magnetic tissue heterogeneity on
 490 the cellular microscale (*Kiselev and Novikov, 2018; Yablonskiy and Haacke, 1994*). In particular, the
 491 heterogeneous distribution of paramagnetic iron among different cell types (*Zecca et al., 2004b;*
 492 *Morawski et al., 2015*) strongly impacts the MRI signal. Larmor frequency perturbations caused by
 493 iron-rich cells induce MRI signal dephasing and therefore signal decay (*Duyn and Schenck, 2017*).

The resulting relaxation rates depend on the spatial distribution of tissue iron and diffusion of
 water molecules through regions with a spatially varying Larmor frequency (*Kiselev and Novikov,*
2018). In the general case, the GE and SE decay contributions from microscale processes can be
 described by

$$\exp\left(-\int_0^{T_E} dt R_{2,micro}^*\right) = \left\langle \exp\left(-\frac{i}{2\pi} \int_0^{T_E} dt \Delta f(\mathbf{r}(t))\right) \right\rangle_{\mathbf{r}}, \quad (4)$$

$$\exp\left(-\int_0^{T_E} dt R_{2,micro}\right) = \left\langle \exp\left(-\frac{i}{2\pi} \left(\int_0^{T_E/2} dt \Delta f(\mathbf{r}(t)) - \int_{T_E/2}^{T_E} dt \Delta f(\mathbf{r}(t))\right)\right) \right\rangle_{\mathbf{r}}, \quad (5)$$

¹¹This is a plausible assumption as the correlation times on the two scales differ by several orders of magnitude: Assuming a tissue diffusion coefficient of $D = 1 \mu\text{m}^2/\text{ms}$, the diffusion times $\tau_D = l^2/D$ across nano- ($l = 10 \text{ nm}$) and microscale ($l = 10 \mu\text{m}$) distances are 100 ns, and 10 ms, respectively.

¹²We derived $r_{2,FT}$ by evaluating the linear relation for R_2 in Fig. 1A in (*Gossuin et al., 2000*) at 7 T and converting mmol l^{-1} to ppm with a density of 1 kg l^{-1} . We derived $r_{2,NM}$ by evaluating the linear relation for r_2 in (*Trujillo et al., 2017*) at 1 ppm and scaling it linearly from 3 T to 7 T.

494 respectively, where Δf is the iron-induced Larmor frequency perturbation and $\mathbf{r}(t)$ the coordinate
 495 of a diffusing water proton spin. The averaging in Eqs. (4) and (5) is performed over the diffusion
 496 paths of all water protons within the MRI voxel, which cannot be performed analytically in the
 497 general case. Instead, numerical Monte Carlo simulations can predict MRI signal decays for arbitrary
 498 distributions of magnetic perturbers and tissue diffusion properties (*Gagnon et al., 2015*). For the
 499 two limiting cases of slow and fast diffusion, Eqs. (4) and (5) analytical solutions were reported.

500 In the case of negligible diffusion,¹³ the static dephasing approximation is applicable. In this case,
 501 the microscale contribution to the transverse relaxation rate $R_{2,\text{micro}}$ is zero and only an effective
 502 transverse relaxation rate $R_{2,\text{micro}}^*$ is induced. If the water protons remain static, the path integral
 503 in Eq. (4) simplifies to the Fourier transformation of the Larmor frequency probability density
 504 $\rho(\Delta f)$ (*Marques and Bowtell, 2005*), which can be estimated from the intravoxel Larmor frequency
 505 histogram (Fig. 4A).

$$\exp\left(-\int_0^{T_E} dt R_{2,\text{micro}}^*\right) = \int_{-\infty}^{\infty} d(\Delta f) \rho(\Delta f) e^{-i/2\pi\Delta f t}. \quad (6)$$

506 In the special case of Larmor frequency perturbations caused by localized magnetic inclusions of
 507 simple geometry (here, iron-rich dopaminergic neurons), the analytical solution of Eq. (6) provides a
 508 quantitative link between the susceptibility of DN and $R_{2,\text{micro}}^*$. As was demonstrated by Yablonskiy
 509 and Haacke (*Yablonskiy and Haacke, 1994*), spherical magnetic inclusions contribute to $R_{2,\text{micro}}^*$ according
 510 to

$$R_{2,\text{micro}}^* = \frac{2\pi}{9\sqrt{3}} \gamma B_0 \cdot \zeta \Delta\chi, \quad (7)$$

511 where ζ is the volume fraction of the magnetic inclusions and $\Delta\chi$ is the difference in susceptibility
 512 between the inclusions and the surrounding tissue. Importantly, the contribution of magnetic
 513 inclusions to $R_{2,\text{micro}}^*$ is proportional to the product of their volume fraction and their susceptibility
 514 difference to the surrounding tissue.

In the opposite limiting case of fast diffusion, an analytic solution for arbitrary local mag-
 netic field perturbations is provided by an effective medium theory for the motional narrowing
 regime (*Novikov and Kiselev, 2008*). The effective medium theory approximates the signal by the
 first terms of a series expansion in the parameter $\alpha = 2\pi\sqrt{\langle\Delta f^2\rangle} \cdot T_E$, which has to be much smaller
 than one for the series to converge. In this case, the contribution to $R_{2,\text{micro}}$ and $R_{2,\text{micro}}^*$ are compa-
 rable. They are determined by the angular-averaged spatial two-point correlation function of the
 iron-induced Larmor frequency perturbation $\bar{\Gamma}_{2,\Delta f}(k)$ in the Fourier domain (*Kiselev and Novikov,*
 2002) (Fig. 4B).¹⁴

$$\exp\left(-\int_0^{T_E} dt R_{2,\text{micro}}^*\right) = \exp\left(-\int_0^{T_E} dt \int \frac{d^3 k}{(2\pi)^3} \bar{\Gamma}_{2,\Delta f}(k) g_{\text{GE}}\right), \quad (8)$$

$$\exp\left(-\int_0^{T_E} dt R_{2,\text{micro}}\right) = \exp\left(-\int_0^{T_E} dt \int \frac{d^3 k}{(2\pi)^3} \bar{\Gamma}_{2,\Delta f}(k) g_{\text{SE}}\right). \quad (9)$$

515 The function $g_{\text{GE/SE}}$ describes the diffusion averaging and is given by $g_{\text{GE}} = 1 - e^{-Dk^2 t}$ and $g_{\text{SE}} =$
 516 $1 - 2e^{-Dk^2 t/2} + e^{-Dk^2 t}$ for GE and SE decays, respectively, where D is the diffusion constant (*Kiselev*
 517 *and Novikov, 2002*).

518 Software Implementation

519 The biophysical model was predominantly implemented using the Python programming language
 520 (Python Software Foundation, <https://www.python.org/>). A previously published Monte Carlo
 521 simulation (*Gagnon et al., 2015*) was re-implemented in the C programming language and run with
 522 10^6 protons and a 0.1 ms time step. The diffusion constant was set to $D = 0.3 \mu\text{m}^2/\text{ms}$ *post mortem*
 523 and $D = 1 \mu\text{m}^2/\text{ms}$ *in vivo* (*Miller et al., 2012*). Relaxation rates were calculated with the same
 524 procedure as for experimental MRI data, using the experimental echo times for fitting (see below).

¹³Negligible and fast diffusion here mean that the time scale of signal dephasing is much shorter and longer, respectively,
 than the diffusion time over the length scale of magnetic inhomogeneities (*Yablonskiy and Haacke, 1994*).

¹⁴To improve readability, $\bar{\Gamma}_{2,\Delta f}$ is referred to as two-point correlator in the main text of this article.

525 **Post mortem Human Brain Tissue Samples**

526 Three midbrain samples (samples 1-3) including *substantia nigra* from human *post mortem* brains
527 were provided by the Brain Banking Centre Leipzig of the German Brain Net (GZ 01GI9999-01GI0299),
528 operated by Paul Flechsig Institute of Brain Research (Approval # 82-02). Sample 1, used in the
529 iron tissue extraction experiment and for biophysical modeling, was donated by a 57-y-old male
530 subject and contained bilateral SN. The samples 2 and 3 contained the left SN from a 86-y-old
531 and a 61-y-old male subject, respectively. The causes of death of the donors of samples 1, 2, and
532 3 were liver failure, heart failure, and renal failure, respectively. Brain material was obtained at
533 autopsy with prior informed consent and approved by the responsible authorities. The *post mortem*
534 interval before fixation was less than 24 h for all tissue samples. Following the standard Brain Bank
535 procedures, blocks were immersion-fixed in 4 % paraformaldehyde in phosphate buffered saline
536 (PBS) at pH 7.4 for at least six weeks to ensure complete fixation. Prior to MRI experiments, tissue
537 blocks were washed in PBS with 0.1 % sodium azide to remove formaldehyde residues from the
538 tissue.

539 **Quantitative MRI**

540 Fixed tissue samples were placed in acrylic spheres of 6 cm diameter and immersed in Fomblin
541 (Solvay Solexis, Bollate, Italy) to eliminate background MRI signal. MRI scanning was performed
542 on a Siemens Magnetom 7 T whole-body MRI scanner (Siemens Healthineers, Erlangen) using a
543 custom-built two-channel quadrature coil designed for imaging small samples. 3D high resolution
544 quantitative multi-parametric mapping (*Weiskopf et al., 2013*) was performed with the following
545 parameters: A 3D multi-echo fast low-angle shot (FLASH) (*Haase et al., 2011*) with field of view
546 (FOV) $32 \times 32 \times 25 \text{ mm}^3$ for the first sample, $50 \times 50 \times 28 \text{ mm}^3$ for the other samples; matrix size
547 $144 \times 144 \times 112$ for the first sample, $224 \times 224 \times 128$ for the other samples (approximately 220 μm
548 isotropic resolution for all samples); twelve echo times $T_E = 4/7.34/10.68/ \dots /40.74 \text{ ms}$ recorded
549 using bipolar readout; repetition time $T_R = 60 \text{ ms}$; flip angle $\alpha = 27^\circ$; bandwidth $BW = 344 \text{ Hz/pixel}$. A
550 single-slice 2D high resolution spin echo acquisition was performed with the following parameters:
551 FOV $42 \times 42 \text{ mm}^2$ for the first sample, $28 \times 28 \text{ mm}^2$ for the other samples; slice thickness 0.6 mm;
552 matrix size 192×192 for the first sample, 128×128 for the other samples (219 μm isotropic in-
553 plane resolution); six acquisitions with $T_E = 15/25/35/45/55/75 \text{ ms}$ for the first sample, and with
554 $T_E = 11/16/25/37/56/83 \text{ ms}$ for the other samples; $T_R = 2 \text{ s}$; $\alpha = 27^\circ$; $BW = 344 \text{ Hz/pixel}$. 3D ultra-high
555 resolution T_2^* -WI was performed using a single-echo FLASH with the following parameters: FOV
556 $46 \times 37 \times 14 \text{ mm}^3$; matrix size $896 \times 728 \times 287$ ($51 \times 51 \times 49 \mu\text{m}^3$ resolution); $T_E = 19.7 \text{ ms}$; $T_R = 180 \text{ ms}$;
557 $\alpha = 48^\circ$; $BW = 40 \text{ Hz/pixel}$; partial Fourier 6/8. All magnitude and phase images were reconstructed
558 and stored. Quantitative parameter maps of R_2^* and R_2 were calculated from the magnitude images
559 using a linear-exponential fit with a Rician noise floor implemented in Python.

560 **Iron Extraction Experiment**

561 After the MRI acquisition, the posterior part of the left SN from sample 1 was soaked in a solution of
562 2 % deferoxamine and 2 % sodium dithionite for 15 days at 37 °C to remove iron from the tissue. The
563 solution was changed every three days. After iron extraction,¹⁵ the MRI acquisition was performed
564 on this sample with the same parameters as before. The ROIs of N1 and N3 were segmented by
565 an anatomy expert (M. M.) on the ultra-high resolution T_2^* -WI acquired before iron extraction. A
566 rigid landmark registration between the MRI data acquired before and after iron extraction was
567 performed.

568 **Histology and Immunohistochemistry**

569 Tissue blocks were embedded in paraffin (Histowax, SAV LP, Flintsbach) and cut into 10 μm sections
570 using a sliding microtome (Jung Histoslide 2000, Leica, Wetzlar). Block-face imaging was used for

¹⁵No metals were present in the tissue after iron extraction, as checked with PIXE measurements.

571 initial co-registration between histology and MRI. The sections were transferred to Superfrost®Plus
572 glass slides (Thermo Fisher Scientific, Massachusetts). For sample 1, ten consecutive sections
573 containing the right *substantia nigra* with visible neuromelanin-pigmented nigrosomes N1 and N3
574 were stained with Perls' stain for iron in order to generate 3D quantitative iron maps. Deparaffinized
575 sections were incubated for 2 h at 37 °C in Perls' working solution, before they were washed in PBS
576 and Tris-HCl. Prior to the 3,3'-diaminobenzidine (DAB) reaction, the sections were preincubated with
577 0.5 mg DAB per ml Tris-HCl. After a 10 min DAB visualization reaction, the sections were washed in Tris-
578 HCl, PBS, and distilled water before they were embedded in Entellan (Merck Millipore, Darmstadt).¹⁶
579 The sections were examined on an AxioScan.Z1 microscope (Zeiss, Jena) with a 20× objective lens
580 (NA 0.5) with the same imaging parameters for all slides and no gamma correction. The images
581 were precisely co-registered to the ultra-high resolution T_2^* -WI with vessels as landmarks (Fig. 1B, C)
582 using the 3D Slicer software (<https://www.slicer.org/>). For samples 2 and 3, a section was stained
583 with Perls' stain. For all samples, the sections adjacent to the Perls' stained sections were used for
584 PIXE. Consecutive sections were stained with Luxol fast blue to localize myelinated fibers and with
585 calbindin antibody for additional nigrosome verification.

586 **PIXE Iron Quantification**

587 PIXE was used to acquire quantitative iron maps (*Ryan, 2011*). Sections from all samples were
588 deparaffinized, embedded in mounting medium (DePeX, Merck Millipore, Darmstadt), and sub-
589 sequently placed into aluminum frames. Prior to PIXE, light microscopy was performed on the
590 framed sections using an Axio Imager 2 microscope (Zeiss, Jena). The images were registered
591 to ultra-high resolution T_2^* -WI as above. For sample 1, PIXE was performed at the Leipzig ion
592 beam laboratory (LIPSION, Leipzig University, Leipzig) using a proton beam of 2.25 MeV and 0.5 nA
593 with a diameter of 0.8 μm . It locally knocked out inner shell electrons, leading to element-specific
594 X-ray emission. Rutherford backscattering spectra were recorded for absolute concentration cal-
595 culations. PIXE was performed on four ROIs in N1 with the following parameters: matrix size
596 1000 × 1000/1000 × 1000/500 × 1500/1600 × 400; FOV 800 × 800/400 × 400/400 × 1600/1600 × 400 μm^2 ;
597 deposited charge 3.1/6.7/2.3/6.7 μC . For samples 2 and 3, PIXE was performed at the Microana-
598 lytical Center (Department for Low and Medium Energy Physics, Jožef Stefan Institute, Ljubljana)
599 using a proton beam of 3.03 MeV and 100 pA to 150 pA with a diameter of 1.5 μm . The measurement
600 parameters were: matrix size 256 × 256 for both; FOV 560 × 560/400 × 400 μm^2 ; deposited charge
601 10.23/6.45 μC . Quantitative iron and sulfur maps were obtained using the GeoPIXE II software (CSIRO,
602 Clayton), following (*Morawski et al., 2015*). These elemental maps were corrected to account for
603 tissue shrinkage during paraffin embedding. A volume shrinkage factor of (0.76 ± 0.02) was found
604 by comparing the distance between vessels on ultra-high resolution T_2^* -WI on sample 1 with their
605 distance in histology.

606 **Iron Quantification in Neuromelanin**

607 Light microscopy and PIXE were combined to determine the local iron concentration in neurome-
608 lanin of dopaminergic neurons and in ferritin outside of DN. DN were identified on microscopy
609 images as brown neuromelanin domains, which most DN contain, especially the ones vulnerable
610 in PD (*Herrero et al., 1993*). Microscopy images were co-registered to the PIXE measurements
611 using elemental sulfur maps on which the sulfur-containing neuromelanin showed up. Probability
612 maps of DN were obtained from semi-automatic segmentation on the microscopy images using
613 fastER (*Hilsenbeck et al., 2017*). After thresholding at 50%, morphological opening with a $2 \times 2 \mu\text{m}^2$
614 kernel was performed to remove small masking artifacts. The local iron concentrations associated
615 with neuromelanin and ferritin were estimated from averaging quantitative PIXE iron maps inside
616 and outside of the DN mask, respectively. The overlap of the PIXE measurement areas on sample 1
617 (Fig. S1D1) was taken into account in the analysis by first averaging over the overlapping areas and
618 second over the whole measurement area.

¹⁶For further details on the staining process, see (*Weigelt, 2019*).

619 **Generation of 3D Quantitative Iron Maps**

620 3D quantitative iron maps of N1 were obtained by calibrating semi-quantitative iron maps generated
621 from Perls' stain with local iron concentrations from PIXE, and subsequent co-registration. Semi-
622 quantitative iron maps were obtained from microscopy images of Perls'-stained sections by applying
623 the Lambert Beer law to the blue color channel, which showed the highest dynamic range. Next,
624 quantitative maps of the iron concentration associated with neuromelanin in DN and ferritin outside
625 of DN were generated by a separate calibration of semi-quantitative iron maps: The local iron
626 concentration in DN was set to the value extracted from quantitative PIXE iron maps using the
627 subset of DN located directly adjacent to the semi-quantitative iron map's volume. Outside of
628 DN, the mean of the semi-quantitative iron maps in the region of the PIXE measurement areas
629 in N1 in sample 1 (Fig. S1D1) was set to the local iron concentration in ferritin from PIXE. A 3D
630 quantitative iron map of N1 was obtained by co-registration of quantitative iron maps in an ROI
631 containing a part of N1, encompassing a volume of $2.5 \times 2.3 \times 0.1 \text{ mm}^3$. To this end, a rigid registration
632 with shared DN on adjacent sections as landmarks was performed. The volume was cropped to a
633 DN-rich area spanning over four voxels of high resolution quantitative MRI parameter maps in N1,
634 i.e. $440 \times 440 \mu\text{m}^2$.

635 **Informing the Biophysical Model**

636 A susceptibility map was calculated from the 3D quantitative iron map by separately scaling iron
637 concentrations in neuromelanin and ferritin with the effective susceptibilities of neuromelanin-
638 bound iron (3.3 ppb/ppm, Supplementary Information) and ferritin-bound iron (1.3 ppb/ppm (*Schenck,*
639 *1992*)), respectively.¹⁷ This map was transformed to an evenly spaced coordinate grid with a
640 resolution of $0.88 \mu\text{m}$ using BSpline interpolation in SimpleTIK (*Lowekamp et al., 2013*).

641 The 3D Larmor frequency shift in N1, used in Monte Carlo simulations (Fig. 5C, D) as well as to
642 determine the Larmor frequency histogram (Fig. 5A), was obtained by convolving the 3D quantitative
643 susceptibility map with a dipole kernel (*Marques and Bowtell, 2005*).

644 The 3D spatial two-point correlation function of the Larmor frequency was calculated using
645 $\Gamma_{2,\Delta f}(\mathbf{k}) = |\Delta f(\mathbf{k})|^2 / V$, where V is the map's volume. After controlling its isotropy, the 3D two-point
646 correlation function was angularly averaged in the plane corresponding to microscopy to estimate
647 the two-point correlator.

648 Modeling the microscale relaxation induced by iron in only one chemical form was based on
649 modified 3D iron maps: For relaxation due to DN, the iron concentration outside of DN was set to
650 the average concentration of ferritin-bound iron. For relaxation due to ferritin-bound iron, the iron
651 concentration in DN was set to the average concentration of ferritin-bound iron.

652 **Acknowledgements**

653 We thank Louis Gagnon and Daniel Mayer for their help with the implementation of Monte Carlo
654 simulations, Anna Jauch for the help with histochemical staining, Nico Scherf for his help with
655 advanced image analysis of histochemical images, Dmitry Novikov and Valerij Kiselev for the
656 discussion on relaxation theory, and Bob Turner for fruitful discussions. M.B. has received funding
657 from the International Max Planck Research School on Neuroscience of Communication: Function,
658 Structure, and Plasticity. The research leading to these results has received funding from the
659 European Research Council under the European Union's Seventh Framework Programme (FP7/2007-
660 2013) / ERC grant agreement n° 616905. N.W. has received funding from the BMBF (01EW1711A &
661 B) in the framework of ERA-NET NEURON. N.W. has received funding from the European Union's
662 Horizon 2020 research and innovation programme under the grant agreement No 681094, and
663 is supported by the Swiss State Secretariat for Education, Research and Innovation (SERI) under
664 contract number 15.0137. Work at JSI was supported by the Slovenian research agency grants
665 No. P1-0112, I0-0005, J7-9398, N1-0090 and EU H2020 project No. 824096 "RADIATE". Aspects

¹⁷For converting volume to mass susceptibility, we used a tissue density of 1 g/cm^3 .

666 of this work were supported by funding from the DFG Priority Program 2041 “Computational
667 Connectomics”, MO 2249/3–1 and the Alzheimer Forschungsinitiative e.V. (AFI #18072) to M.M.

668 Competing interests

669 The Max Planck Institute for Human Cognitive and Brain Sciences has an institutional research agree-
670 ment with Siemens Healthcare. NW was a speaker at an event organized by Siemens Healthcare
671 and was reimbursed for the travel expenses.

672 References

- 673 **Agid Y.** Parkinson’s disease: pathophysiology. *The Lancet*. 1991 Jun; 337(8753):1321–1324. <http://www.sciencedirect.com/science/article/pii/S014067369192989F>, doi: 10.1016/0140-6736(91)92989-F.
- 674
- 675 **Betts MJ,** Kirilina E, Otaduy MCG, Ivanov D, Acosta-Cabronero J, Callaghan MF, Lambert C, Cardenas-Blanco A,
676 Pine K, Passamonti L, Loane C, Keuken MC, Trujillo P, Lüsebrink F, Mattern H, Liu KY, Privoulos N, Fließbach
677 K, Dahl MJ, Maaß A, et al. Locus coeruleus imaging as a biomarker for noradrenergic dysfunction in neu-
678 rodegenerative diseases. *Brain*. 2019 Sep; 142(9):2558–2571. [https://www.ncbi.nlm.nih.gov/pmc/articles/](https://www.ncbi.nlm.nih.gov/pmc/articles/PMC6736046/)
679 [PMC6736046/](https://www.ncbi.nlm.nih.gov/pmc/articles/PMC6736046/), doi: 10.1093/brain/awz193.
- 680 **Birkl C,** Langkammer C, Golob-Schwarzl N, Leoni M, Haybaeck J, Goessler W, Fazekas F, Ropele S. Effects of
681 formalin fixation and temperature on MR relaxation times in the human brain. *NMR in Biomedicine*. 2016
682 Apr; 29(4):458–465. <http://onlinelibrary.wiley.com/doi/10.1002/nbm.3477/abstract>, doi: 10.1002/nbm.3477.
- 683 **Blazejewska AI,** Schwarz ST, Pitiot A, Stephenson MC, Lowe J, Bajaj N, Bowtell RW, Auer DP, Gowland PA.
684 Visualization of nigrosome 1 and its loss in PD Pathoanatomical correlation and in vivo 7 T MRI. *Neurology*.
685 2013 Aug; 81(6):534–540. <http://www.neurology.org/content/81/6/534>, doi: 10.1212/WNL.0b013e31829e6fd2.
- 686 **Brooks RA,** Vymazal J, Goldfarb RB, Bulte JW, Aisen P. Relaxometry and magnetometry of ferritin. *Magnetic*
687 *Resonance in Medicine*. 1998 Aug; 40(2):227–235.
- 688 **Cheng Z,** He N, Huang P, Li Y, Tang R, Sethi SK, Ghassaban K, Yerramsetty KK, Palutla VK, Chen S, Yan F,
689 Haacke EM. Imaging the Nigrosome 1 in the substantia nigra using susceptibility weighted imaging and
690 quantitative susceptibility mapping: An application to Parkinson’s disease. *NeuroImage : Clinical*. 2019 Nov;
691 25. <https://www.ncbi.nlm.nih.gov/pmc/articles/PMC6933220/>, doi: 10.1016/j.nicl.2019.102103.
- 692 **Cho SB,** Kim BJ, Suh BJ, Jang ZH. Comparison of the magnetic properties of natural ferritin with those of
693 aggregated magnetic core of ferritin. *Journal of the Korean Physical Society*. 2004 Aug; 45(2):485–489.
694 http://inis.iaea.org/Search/search.aspx?orig_q=RN:41104970.
- 695 **Cosottini M,** Frosini D, Pesaresi I, Costagli M, Biagi L, Ceravolo R, Bonuccelli U, Tosetti M. MR imaging of the
696 substantia nigra at 7 T enables diagnosis of Parkinson disease. *Radiology*. 2014 Jun; 271(3):831–838. doi:
697 10.1148/radiol.14131448.
- 698 **Craelius W,** Migdal MW, Luessenhop CP, Sugar A, Mihalakis I. Iron deposits surrounding multiple sclerosis
699 plaques. *Archives of Pathology & Laboratory Medicine*. 1982 Aug; 106(8):397–399.
- 700 **Damier P,** Hirsch EC, Agid Y, Graybiel AM. The substantia nigra of the human brain. I. Nigrosomes and the
701 nigral matrix, a compartmental organization based on calbindin D(28K) immunohistochemistry. *Brain*. 1999;
702 122(8):1421–1436. <http://europemc.org/abstract/med/10430829>, doi: 10.1093/brain/122.8.1421.
- 703 **Damier P,** Hirsch EC, Agid Y, Graybiel AM. The substantia nigra of the human brain. II. Patterns of loss of
704 dopamine-containing neurons in Parkinson’s disease. *Brain: A Journal of Neurology*. 1999 Aug; 122(8):1437–
705 1448.
- 706 **Deistung A,** Schäfer A, Schweser F, Biedermann U, Turner R, Reichenbach JR. Toward in vivo histology: A
707 comparison of quantitative susceptibility mapping (QSM) with magnitude-, phase-, and R2*-imaging at ultra-
708 high magnetic field strength. *NeuroImage*. 2013 Jan; 65:299–314. [http://www.sciencedirect.com/science/](http://www.sciencedirect.com/science/article/pii/S1053811912009652)
709 [article/pii/S1053811912009652](http://www.sciencedirect.com/science/article/pii/S1053811912009652), doi: 10.1016/j.neuroimage.2012.09.055.
- 710 **Dexter DT,** Carayon A, Javoy-Agid F, Agid Y, Wells FR, Daniel SE, Lees AJ, Jenner P, Marsden CD. Alterations in the
711 levels of iron, ferritin and other trace metals in Parkinson’s disease and other neurodegenerative diseases
712 affecting the basal ganglia. *Brain*. 1991 Aug; 114(4):1953–1975. [https://academic.oup.com/brain/article/114/](https://academic.oup.com/brain/article/114/4/1953/387366)
713 [4/1953/387366](https://academic.oup.com/brain/article/114/4/1953/387366), doi: 10.1093/brain/114.4.1953.

- 714 **Dexter DT**, Wells FR, Lee AJ, Agid F, Agid Y, Jenner P, Marsden CD. Increased Nigral Iron Content and Alterations
715 in Other Metal Ions Occurring in Brain in Parkinson's Disease. *Journal of Neurochemistry*. 1989; 52(6):1830–
716 1836. <https://onlinelibrary.wiley.com/doi/abs/10.1111/j.1471-4159.1989.tb07264.x>, doi: 10.1111/j.1471-
717 4159.1989.tb07264.x.
- 718 **Duyn JH**, Schenck J. Contributions to magnetic susceptibility of brain tissue. *NMR in biomedicine*. 2017 Apr;
719 30(4):1–37. <https://www.ncbi.nlm.nih.gov/pmc/articles/PMC5131875/>, doi: 10.1002/nbm.3546.
- 720 **Edwards LJ**, Kirilina E, Mohammadi S, Weiskopf N. Microstructural imaging of human neocortex in vivo.
721 *NeuroImage*. 2018 Nov; 182:184–206. <http://www.sciencedirect.com/science/article/pii/S1053811918301629>,
722 doi: 10.1016/j.neuroimage.2018.02.055.
- 723 **Fukunaga M**, Li TQ, van Gelderen P, de Zwart JA, Shmueli K, Yao B, Lee J, Maric D, Aronova MA, Zhang G, Leapman
724 RD, Schenck JF, Merkle H, Duyn JH. Layer-specific variation of iron content in cerebral cortex as a source of
725 MRI contrast. *Proceedings of the National Academy of Sciences of the United States of America*. 2010 Feb;
726 107(8):3834–3839. <https://www.ncbi.nlm.nih.gov/pmc/articles/PMC2840419/>, doi: 10.1073/pnas.0911177107.
- 727 **Gagnon L**, Sakadžić S, Lesage F, Musacchia JJ, Lefebvre J, Fang Q, Yücel MA, Evans KC, Mandeville ET, Cohen-
728 Adad J, Polimeni JR, Yaseen MA, Lo EH, Greve DN, Buxton RB, Dale AM, Devor A, Boas DA. Quantifying the
729 microvascular origin of BOLD-fMRI from first principles with two-photon microscopy and an oxygen-sensitive
730 nanoprobe. *The Journal of Neuroscience: The Official Journal of the Society for Neuroscience*. 2015 Feb;
731 35(8):3663–3675. doi: 10.1523/JNEUROSCI.3555-14.2015.
- 732 **Galazka-Friedman J**, Bauminger ER, Friedman A, Barcikowska M, Hechel D, Nowik I. Iron in parkinsonian
733 and control substantia nigra—A mössbauer spectroscopy study. *Movement Disorders*. 1996; 11(1):8–16.
734 <https://onlinelibrary.wiley.com/doi/abs/10.1002/mds.870110104>, doi: 10.1002/mds.870110104.
- 735 **Gossuin Y**, Roch A, Muller RN, Gillis P. Relaxation induced by ferritin and ferritin-like magnetic particles: The
736 role of proton exchange. *Magnetic Resonance in Medicine*. 2000; 43(2):237–243. doi: 10.1002/(SICI)1522-
737 2594(200002)43:2<237::AID-MRM10>3.0.CO;2-5.
- 738 **Gossuin Y**, Roch A, Muller RN, Gillis P, Lo Bue F. Anomalous nuclear magnetic relaxation of aqueous solutions of
739 ferritin: An unprecedented first-order mechanism. *Magnetic Resonance in Medicine*. 2002 Dec; 48(6):959–964.
740 <http://onlinelibrary.wiley.com/doi/10.1002/mrm.10316/abstract>, doi: 10.1002/mrm.10316.
- 741 **Haacke EM**, Cheng NYC, House MJ, Liu Q, Neelavalli J, Ogg RJ, Khan A, Ayaz M, Kirsch W, Obenaus A. Imaging iron
742 stores in the brain using magnetic resonance imaging. *Magnetic Resonance Imaging*. 2005 Jan; 23(1):1–25.
743 <http://www.sciencedirect.com/science/article/pii/S0730725X04002905>, doi: 10.1016/j.mri.2004.10.001.
- 744 **Haase A**, Frahm J, Matthaei D, Hänicke W, Merboldt KD. FLASH imaging: Rapid NMR imaging using low flip-angle
745 pulses. *Journal of Magnetic Resonance*. 2011 Dec; 213(2):533–541. [http://www.sciencedirect.com/science/
746 article/pii/S1090780711003338](http://www.sciencedirect.com/science/article/pii/S1090780711003338), doi: 10.1016/j.jmr.2011.09.021.
- 747 **Hallgren B**, Sourander P. The Effect of Age on the Non-Haemin Iron in the Human Brain. *Journal of Neurochem-*
748 *istry*. 1958 Oct; 3(1):41–51. <http://onlinelibrary.wiley.com/doi/10.1111/j.1471-4159.1958.tb12607.x/abstract>,
749 doi: 10.1111/j.1471-4159.1958.tb12607.x.
- 750 **Herrero MT**, Hirsch EC, Kastner A, Ruberg M, Luquin MR, Laguna J, Javoy-Agid F, Obeso JA, Agid Y. Does
751 neuromelanin contribute to the vulnerability of catecholaminergic neurons in monkeys intoxicated with
752 MPTP? *Neuroscience*. 1993 Sep; 56(2):499–511. doi: 10.1016/0306-4522(93)90349-k.
- 753 **Hilsenbeck O**, Schwarzfischer M, Loeffler D, Dimopoulos S, Hastreiter S, Marr C, Theis FJ, Schroeder T. fastER: a
754 user-friendly tool for ultrafast and robust cell segmentation in large-scale microscopy. *Bioinformatics*. 2017
755 Jul; 33(13):2020–2028. doi: 10.1093/bioinformatics/btx107.
- 756 **Isaias IU**, Trujillo P, Summers P, Marotta G, Mainardi L, Pezzoli G, Zecca L, Costa A. Neuromelanin Imag-
757 ing and Dopaminergic Loss in Parkinson's Disease. *Frontiers in Aging Neuroscience*. 2016; 8:196. doi:
758 10.3389/fnagi.2016.00196.
- 759 **Kakhlon O**, Cabantchik ZI. The labile iron pool: characterization, measurement, and participation in cellular
760 processes. *Free Radical Biology and Medicine*. 2002 Oct; 33(8):1037–1046. [http://www.sciencedirect.com/
761 science/article/pii/S0891584902010067](http://www.sciencedirect.com/science/article/pii/S0891584902010067), doi: 10.1016/S0891-5849(02)01006-7.
- 762 **Kiselev VG**, Novikov DS. Transverse NMR relaxation as a probe of mesoscopic structure. *Physical Review Letters*.
763 2002 Dec; 89(27):278101. doi: 10.1103/PhysRevLett.89.278101.

- 764 **Kiselev VG**, Novikov DS. Transverse NMR relaxation in biological tissues. *NeuroImage*. 2018
765 Nov; 182:149–168. <http://www.sciencedirect.com/science/article/pii/S1053811918305093>, doi:
766 [10.1016/j.neuroimage.2018.06.002](https://doi.org/10.1016/j.neuroimage.2018.06.002).
- 767 **Kwon DH**, Kim JM, Oh SH, Jeong HJ, Park SY, Oh ES, Chi JG, Kim YB, Jeon BS, Cho ZH. Seven-tesla magnetic
768 resonance images of the substantia nigra in Parkinson disease. *Annals of Neurology*. 2012 Feb; 71(2):267–277.
769 <http://onlinelibrary.wiley.com/doi/10.1002/ana.22592/abstract>, doi: [10.1002/ana.22592](https://doi.org/10.1002/ana.22592).
- 770 **Langkammer C**, Pirpamer L, Seiler S, Deistung A, Schweser F, Franthal S, Homayoon N, Katschnig-Winter P, Koegl-
771 Wallner M, Pendl T, Stoegerer EM, Wenzel K, Fazekas F, Ropele S, Reichenbach JR, Schmidt R, Schwingenschuh
772 P. Quantitative Susceptibility Mapping in Parkinson's Disease. *PLoS ONE*. 2016 Sep; 11(9). <http://www.ncbi.nlm.nih.gov/pmc/articles/PMC5012676/>, doi: [10.1371/journal.pone.0162460](https://doi.org/10.1371/journal.pone.0162460).
- 774 **Langkammer C**, Schweser F, Krebs N, Deistung A, Goessler W, Scheurer E, Sommer K, Reishofer G, Yen K,
775 Fazekas F, Ropele S, Reichenbach JR. Quantitative susceptibility mapping (QSM) as a means to measure brain
776 iron? A post mortem validation study. *NeuroImage*. 2012 Sep; 62(3):1593–1599. <http://www.sciencedirect.com/science/article/pii/S105381191200537X>, doi: [10.1016/j.neuroimage.2012.05.049](https://doi.org/10.1016/j.neuroimage.2012.05.049).
- 778 **Lee H**, Baek SY, Chun SY, Lee JH, Cho H. Specific visualization of neuromelanin-iron complex and ferric iron in the
779 human post-mortem substantia nigra using MR relaxometry at 7T. *NeuroImage*. 2018 May; 172:874–885. <http://www.sciencedirect.com/science/article/pii/S1053811917309679>, doi: [10.1016/j.neuroimage.2017.11.035](https://doi.org/10.1016/j.neuroimage.2017.11.035).
- 781 **Lee H**, Baek SY, Kim EJ, Huh GY, Lee JH, Cho H. MRI T2 and T2* relaxometry to visualize neuromelanin in the dorsal
782 substantia nigra pars compacta. *NeuroImage*. 2020 Feb; 211:116625. doi: [10.1016/j.neuroimage.2020.116625](https://doi.org/10.1016/j.neuroimage.2020.116625).
- 783 **Lee JH**, Baek SY, Song Y, Lim S, Lee H, Nguyen MP, Kim EJ, Huh GY, Chun SY, Cho H. The Neuromelanin-related
784 T2* Contrast in Postmortem Human Substantia Nigra with 7T MRI. *Scientific Reports*. 2016 Sep; 6:srep32647.
785 <https://www.nature.com/articles/srep32647>, doi: [10.1038/srep32647](https://doi.org/10.1038/srep32647).
- 786 **Léhéricy S**, Bardin E, Poupon C, Vidailhet M, François C. 7 tesla magnetic resonance imaging: A closer look
787 at substantia nigra anatomy in Parkinson's disease. *Movement Disorders*. 2014 Nov; 29(13):1574–1581.
788 <http://onlinelibrary.wiley.com/doi/10.1002/mds.26043/abstract>, doi: [10.1002/mds.26043](https://doi.org/10.1002/mds.26043).
- 789 **Loeffler DA**, Connor JR, Juneau PL, Snyder BS, Kanaley L, DeMaggio AJ, Nguyen H, Brickman CM, LeWitt PA.
790 Transferrin and Iron in Normal, Alzheimer's Disease, and Parkinson's Disease Brain Regions. *Journal of*
791 *Neurochemistry*. 2002 Nov; 65(2):710–716. <http://doi.wiley.com/10.1046/j.1471-4159.1995.65020710.x>, doi:
792 [10.1046/j.1471-4159.1995.65020710.x](https://doi.org/10.1046/j.1471-4159.1995.65020710.x).
- 793 **Lowekamp BC**, Chen DT, Ibáñez L, Blezek D. The Design of SimpleITK. *Frontiers in Neuroinformatics*. 2013; 7:45.
794 doi: [10.3389/fninf.2013.00045](https://doi.org/10.3389/fninf.2013.00045).
- 795 **Lüsebrink F**, Sciarra A, Mattern H, Yakupov R, Speck O. T1 -weighted in vivo human whole brain MRI dataset
796 with an ultrahigh isotropic resolution of 250 micro meter. *Scientific Data*. 2017 Mar; 4(1):1–12. <https://www.nature.com/articles/sdata201732>, doi: [10.1038/sdata.2017.32](https://doi.org/10.1038/sdata.2017.32).
- 798 **Mahlknecht P**, Krismer F, Poewe W, Seppi K. Meta-analysis of dorsolateral nigral hyperintensity on magnetic
799 resonance imaging as a marker for Parkinson's disease. *Movement Disorders: Official Journal of the Movement*
800 *Disorder Society*. 2017; 32(4):619–623. doi: [10.1002/mds.26932](https://doi.org/10.1002/mds.26932).
- 801 **Marques Jp**, Bowtell R. Application of a Fourier-based method for rapid calculation of field inhomogeneity due
802 to spatial variation of magnetic susceptibility. *Concepts in Magnetic Resonance Part B: Magnetic Resonance*
803 *Engineering*. 2005 Apr; 25B(1):65–78. <http://onlinelibrary.wiley.com/doi/10.1002/cmr.b.20034/abstract>, doi:
804 [10.1002/cmr.b.20034](https://doi.org/10.1002/cmr.b.20034).
- 805 **Meadowcroft MD**, Peters DG, Dewal RP, Connor JR, Yang QX. The effect of iron in MRI and transverse relaxation
806 of amyloid-beta plaques in Alzheimer's disease. *NMR in Biomedicine*. 2015 Mar; 28(3):297–305. <http://onlinelibrary.wiley.com/doi/10.1002/nbm.3247/abstract>, doi: [10.1002/nbm.3247](https://doi.org/10.1002/nbm.3247).
- 808 **Metere R**, Kober T, Möller HE, Schäfer A. Simultaneous Quantitative MRI Mapping of T1, T2* and Magnetic
809 Susceptibility with Multi-Echo MP2RAGE. *PLoS ONE*. 2017 Jan; 12(1):e0169265. <https://journals.plos.org/plosone/article?id=10.1371/journal.pone.0169265>, doi: [10.1371/journal.pone.0169265](https://doi.org/10.1371/journal.pone.0169265).
- 811 **Miller KL**, McNab JA, Jbabdi S, Douaud G. Diffusion tractography of post-mortem human brains: Op-
812 timization and comparison of spin echo and steady-state free precession techniques. *NeuroImage*.
813 2012 Feb; 59(3):2284–2297. <http://www.sciencedirect.com/science/article/pii/S1053811911011281>, doi:
814 [10.1016/j.neuroimage.2011.09.054](https://doi.org/10.1016/j.neuroimage.2011.09.054).

- 815 **Morawski M**, Meinecke C, Reinert T, Dörfel AC, Riederer P, Arendt T, Butz T. Determination of trace elements
816 in the human substantia nigra. *Nuclear Instruments and Methods in Physics Research Section B: Beam*
817 *Interactions with Materials and Atoms*. 2005 Apr; 231:224–228. doi: [10.1016/j.nimb.2005.01.061](https://doi.org/10.1016/j.nimb.2005.01.061).
- 818 **Morawski M**, Reinert T, Meyer-Klaucke W, Wagner FE, Tröger W, Reinert A, Jäger C, Brückner G, Arendt T. Ion
819 exchanger in the brain: Quantitative analysis of perineuronally fixed anionic binding sites suggests diffusion
820 barriers with ion sorting properties. *Scientific Reports*. 2015 Dec; 5. [https://www.ncbi.nlm.nih.gov/pmc/](https://www.ncbi.nlm.nih.gov/pmc/articles/PMC4664884/)
821 [articles/PMC4664884/](https://www.ncbi.nlm.nih.gov/pmc/articles/PMC4664884/), doi: 10.1038/srep16471.
- 822 **Novikov DS**, Kiselev VG. Transverse NMR relaxation in magnetically heterogeneous media. *Journal of Magnetic*
823 *Resonance*. 2008 Nov; 195(1):33–39. <http://www.sciencedirect.com/science/article/pii/S1090780708002644>,
824 doi: 10.1016/j.jmr.2008.08.005.
- 825 **Péran P**, Cherubini A, Assogna F, Piras F, Quattrocchi C, Peppe A, Celsis P, Rascol O, Démonet JF, Stefani A,
826 Pierantozzi M, Pontieri FE, Caltagirone C, Spalletta G, Sabatini U. Magnetic resonance imaging markers of
827 Parkinson's disease nigrostriatal signature. *Brain*. 2010 Nov; 133(11):3423–3433. [https://academic.oup.com/](https://academic.oup.com/brain/article/133/11/3423/313450)
828 [brain/article/133/11/3423/313450](https://academic.oup.com/brain/article/133/11/3423/313450), doi: 10.1093/brain/awq212.
- 829 **Reinert T**, Fiedler A, Morawski M, Arendt T. High resolution quantitative element mapping of neuromelanin-
830 containing neurons. *Nuclear Instruments and Methods in Physics Research Section B: Beam Interac-*
831 *tions with Materials and Atoms*. 2007 Jul; 260(1):227–230. [http://www.sciencedirect.com/science/article/pii/](http://www.sciencedirect.com/science/article/pii/S0168583X07003722)
832 [S0168583X07003722](http://www.sciencedirect.com/science/article/pii/S0168583X07003722), doi: 10.1016/j.nimb.2007.02.070.
- 833 **Reinert T**, Spemann D, Morawski M, Arendt T. Quantitative trace element analysis with sub-micron lateral
834 resolution. *Nuclear Instruments and Methods in Physics Research Section B: Beam Interactions with Materials*
835 *and Atoms*. 2006 Aug; 249(1):734–737. <http://www.sciencedirect.com/science/article/pii/S0168583X06003648>,
836 doi: 10.1016/j.nimb.2006.03.129.
- 837 **Riederer P**, Sofic E, Rausch WD, Schmidt B, Reynolds GP, Jellinger K, Youdim MBH. Transition Metals, Fer-
838 ritin, Glutathione, and Ascorbic Acid in Parkinsonian Brains. *Journal of Neurochemistry*. 1989; 52(2):515–
839 520. <https://onlinelibrary.wiley.com/doi/abs/10.1111/j.1471-4159.1989.tb09150.x>, doi: 10.1111/j.1471-
840 4159.1989.tb09150.x.
- 841 **Rutledge JN**, Hilal SK, Silver AJ, Defendini R, Fahn S. Study of Movement Disorders and Brain Iron by MR.
842 *American Journal of Neuroradiology*. 1987 May; 8(3):397–411. <http://www.ajnr.org/content/8/3/397>.
- 843 **Ryan CG**. PIXE and the nuclear microprobe: Tools for quantitative imaging of complex natural materials.
844 *Nuclear Instruments and Methods in Physics Research Section B: Beam Interactions with Materials and Atoms*.
845 2011 Oct; 269(20):2151–2162. <http://www.sciencedirect.com/science/article/pii/S0168583X11002291>, doi:
846 10.1016/j.nimb.2011.02.046.
- 847 **Sasaki M**, Shibata E, Tohyama K, Takahashi J, Otsuka K, Tsuchiya K, Takahashi S, Ehara S, Terayama Y, Sakai A.
848 Neuromelanin magnetic resonance imaging of locus ceruleus and substantia nigra in Parkinson's disease.
849 *NeuroReport*. 2006 Jul; 17(11):1215–1218. <https://insights.ovid.com/crossref?an=00001756-200607310-00027>,
850 doi: 10.1097/01.wnr.0000227984.84927.a7.
- 851 **Schenck JF**. Health and Physiological Effects of Human Exposure to Whole-Body Four-Tesla Magnetic Fields
852 during MRI. *Annals of the New York Academy of Sciences*. 1992 Mar; 649(1):285–301. [http://onlinelibrary.](http://onlinelibrary.wiley.com/doi/10.1111/j.1749-6632.1992.tb49617.x/abstract)
853 [wiley.com/doi/10.1111/j.1749-6632.1992.tb49617.x/abstract](http://onlinelibrary.wiley.com/doi/10.1111/j.1749-6632.1992.tb49617.x/abstract), doi: 10.1111/j.1749-6632.1992.tb49617.x.
- 854 **Schenck JF**, Zimmerman EA. High-field magnetic resonance imaging of brain iron: birth of a biomarker? *NMR*
855 *in Biomedicine*. 2004 Nov; 17(7):433–445. <http://doi.wiley.com/10.1002/nbm.922>, doi: 10.1002/nbm.922.
- 856 **Schwarz ST**, Afzal M, Morgan PS, Bajaj N, Gowland PA, Auer DP. The 'Swallow Tail' Appearance of the Healthy
857 Nigrosome – A New Accurate Test of Parkinson's Disease: A Case-Control and Retrospective Cross-Sectional
858 MRI Study at 3T. *PLOS ONE*. 2014 Apr; 9(4):e93814. [https://journals.plos.org/plosone/article?id=10.1371/](https://journals.plos.org/plosone/article?id=10.1371/journal.pone.0093814)
859 [journal.pone.0093814](https://journals.plos.org/plosone/article?id=10.1371/journal.pone.0093814), doi: 10.1371/journal.pone.0093814.
- 860 **Schwarz ST**, Mougín O, Xing Y, Blazejewska A, Bajaj N, Auer DP, Gowland P. Parkinson's disease related signal
861 change in the nigrosomes 1–5 and the substantia nigra using T2* weighted 7T MRI. *NeuroImage : Clinical*. 2018
862 May; 19:683–689. <https://www.ncbi.nlm.nih.gov/pmc/articles/PMC5986169/>, doi: 10.1016/j.nicl.2018.05.027.
- 863 **Schäfer-Nolte EO**. Development of a diamond-based scanning probe spin sensor operating at low temperature
864 in ultra high vacuum. Dissertation, Stuttgart University; 2014.

- 865 **Stucht D**, Danishad KA, Schulze P, Godenschweger F, Zaitsev M, Speck O. Highest Resolution In Vivo Human
866 Brain MRI Using Prospective Motion Correction. *PLOS ONE*. 2015 Jul; 10(7):e0133921. <https://journals.plos.org/plosone/article?id=10.1371/journal.pone.0133921>, doi: 10.1371/journal.pone.0133921.
- 868 **Stüber C**, Morawski M, Schäfer A, Labadie C, Wähnert M, Leuze C, Streicher M, Barapatre N, Reimann K, Geyer S,
869 Spemann D, Turner R. Myelin and iron concentration in the human brain: A quantitative study of MRI contrast.
870 *NeuroImage*. 2014 Jun; 93(1):95–106. <http://www.sciencedirect.com/science/article/pii/S1053811914001359>,
871 doi: 10.1016/j.neuroimage.2014.02.026.
- 872 **Sulzer D**, Cassidy C, Horga G, Kang UJ, Fahn S, Casella L, Pezzoli G, Langley J, Hu XP, Zucca FA, Isaias IU, Zecca L.
873 Neuromelanin detection by magnetic resonance imaging (MRI) and its promise as a biomarker for Parkinson's
874 disease. *NPJ Parkinson's Disease*. 2018 Apr; 4(11). <https://www.ncbi.nlm.nih.gov/pmc/articles/PMC5893576/>,
875 doi: 10.1038/s41531-018-0047-3.
- 876 **Tambasco N**, Paolini Paoletti F, Chiappiniello A, Lisetti V, Nigro P, Eusebi P, Chiarini P, Romoli M, Brahimi E,
877 Simoni S, Filidei M, Floridi P, Tarducci R, Parnetti L, Calabresi P. T2*-weighted MRI values correlate with
878 motor and cognitive dysfunction in Parkinson's disease. *Neurobiology of Aging*. 2019 Aug; 80:91–98. <http://www.sciencedirect.com/science/article/pii/S0197458019301125>, doi: 10.1016/j.neurobiolaging.2019.04.005.
- 880 **Tardif CL**, Schäfer A, Trampel R, Villringer A, Turner R, Bazin PL. Open Science CBS Neuroimaging Repos-
881 itory: Sharing ultra-high-field MR images of the brain. *NeuroImage*. 2016 Jan; 124:1143–1148. <http://www.sciencedirect.com/science/article/pii/S1053811915007612>, doi: 10.1016/j.neuroimage.2015.08.042.
- 883 **Trampel R**, Bazin PL, Pine K, Weiskopf N. In-vivo magnetic resonance imaging (MRI) of laminae in the human
884 cortex. *NeuroImage*. 2019; 197:707–715. doi: 10.1016/j.neuroimage.2017.09.037.
- 885 **Troprès I**, Grimault S, Vaeth A, Grillon E, Julien C, Payen JF, Lamalle L, Décorps M. Vessel size imaging.
886 *Magnetic Resonance in Medicine*. 2001; 45(3):397–408. doi: 10.1002/1522-2594(200103)45:3<397::AID-
887 MRM1052>3.0.CO;2-3.
- 888 **Trujillo P**, Summers PE, Ferrari E, Zucca FA, Sturini M, Mainardi LT, Cerutti S, Smith AK, Smith SA, Zecca L,
889 Costa A. Contrast mechanisms associated with neuromelanin-MRI. *Magnetic Resonance in Medicine*. 2017;
890 78(5):1790–1800. <https://onlinelibrary.wiley.com/doi/abs/10.1002/mrm.26584>, doi: 10.1002/mrm.26584.
- 891 **Ulrich X**, Yablonskiy DA. Separation of Cellular and BOLD Contributions to T2* Signal Relaxation. *Magnetic*
892 *resonance in medicine*. 2016 Feb; 75(2):606–615. <https://www.ncbi.nlm.nih.gov/pmc/articles/PMC4565789/>,
893 doi: 10.1002/mrm.25610.
- 894 **Uludağ K**, Müller-Bierl B, Uğurbil K. An integrative model for neuronal activity-induced signal changes for
895 gradient and spin echo functional imaging. *NeuroImage*. 2009; 48(1):150–165. <http://www.sciencedirect.com/science/article/pii/S1053811909005576>, doi: 10.1016/j.neuroimage.2009.05.051.
- 897 **Vannesjo SJ**, Wilm BJ, Duerst Y, Gross S, Brunner DO, Dietrich BE, Schmid T, Barmet C, Pruessmann KP. Retro-
898 spective correction of physiological field fluctuations in high-field brain MRI using concurrent field monitoring.
899 *Magnetic Resonance in Medicine*. 2015; 73(5):1833–1843. <https://onlinelibrary.wiley.com/doi/abs/10.1002/mrm.25303>, doi: 10.1002/mrm.25303.
- 901 **Versluis MJ**, Peeters JM, van Rooden S, van der Grond J, van Buchem MA, Webb AG, van Osch MJP. Origin and
902 reduction of motion and f0 artifacts in high resolution T2*-weighted magnetic resonance imaging: Application
903 in Alzheimer's disease patients. *NeuroImage*. 2010 Jul; 51(3):1082–1088. <http://www.sciencedirect.com/science/article/pii/S1053811910003356>, doi: 10.1016/j.neuroimage.2010.03.048.
- 905 **Ward RJ**, Zucca FA, Duyn JH, Crichton RR, Zecca L. The role of iron in brain ageing and neurodegenerative
906 disorders. *The Lancet Neurology*. 2014 Oct; 13(10):1045–1060. <https://www.ncbi.nlm.nih.gov/pmc/articles/PMC5672917/>, doi: 10.1016/S1474-4422(14)70117-6.
- 908 **Weigelt I**. Quantifizierung und zelluläre Lokalisation von Eisen im Gehirn von Patienten mit Parkinsonscher
909 Erkrankung und altersgerechten Kontrollen. Dissertation, Leipzig University; 2019.
- 910 **Weiskopf N**, Suckling J, Williams G, Correia MM, Inkster B, Tait R, Ooi C, Bullmore ET, Lutti A. Quantitative
911 multi-parameter mapping of R1, PD*, MT, and R2* at 3T: a multi-center validation. *Frontiers in Neuroscience*.
912 2013; 7:95. <https://www.frontiersin.org/articles/10.3389/fnins.2013.00095/full>, doi: 10.3389/fnins.2013.00095.
- 913 **Wen J**, Goyal MS, Astafiev SV, Raichle ME, Yablonskiy DA. Genetically defined cellular correlates of the baseline
914 brain MRI signal. *Proceedings of the National Academy of Sciences*. 2018 Oct; 115(41):E9727–E9736. <http://www.pnas.org/content/115/41/E9727>, doi: 10.1073/pnas.1808121115.
- 915

- 916 **Wharton S**, Bowtell R. Fiber orientation-dependent white matter contrast in gradient echo MRI. Proceedings of
917 the National Academy of Sciences. 2012 Nov; 109(45):18559–18564. [https://www.pnas.org/content/109/45/](https://www.pnas.org/content/109/45/18559)
918 [18559](https://www.pnas.org/content/109/45/18559), doi: [10.1073/pnas.1211075109](https://doi.org/10.1073/pnas.1211075109).
- 919 **Yablonskiy DA**, Haacke EM. Theory of NMR signal behavior in magnetically inhomogeneous tissues: The static
920 dephasing regime. Magnetic Resonance in Medicine. 1994 Dec; 32(6):749–763. [http://onlinelibrary.wiley.com/](http://onlinelibrary.wiley.com/doi/10.1002/mrm.1910320610/abstract)
921 [doi/10.1002/mrm.1910320610/abstract](http://onlinelibrary.wiley.com/doi/10.1002/mrm.1910320610/abstract), doi: [10.1002/mrm.1910320610](https://doi.org/10.1002/mrm.1910320610).
- 922 **Yao B**, Li TQ, Gelderen Pv, Shmueli K, de Zwart JA, Duyn JH. Susceptibility contrast in high field MRI of human
923 brain as a function of tissue iron content. NeuroImage. 2009 Feb; 44(4):1259–1266. [http://www.sciencedirect.](http://www.sciencedirect.com/science/article/pii/S1053811908011191)
924 [com/science/article/pii/S1053811908011191](http://www.sciencedirect.com/science/article/pii/S1053811908011191), doi: [10.1016/j.neuroimage.2008.10.029](https://doi.org/10.1016/j.neuroimage.2008.10.029).
- 925 **Zecca L**, Stroppolo A, Gatti A, Tampellini D, Toscani M, Gallorini M, Giaveri G, Arosio P, Santambrogio P, Fariello RG,
926 Karatekin E, Kleinman MH, Turro N, Hornykiewicz O, Zucca FA. The role of iron and copper molecules in the neu-
927 ron vulnerability of locus coeruleus and substantia nigra during aging. Proceedings of the National Academy
928 of Sciences of the United States of America. 2004 Jun; 101(26):9843–9848. doi: [10.1073/pnas.0403495101](https://doi.org/10.1073/pnas.0403495101).
- 929 **Zecca L**, Youdim MBH, Riederer P, Connor JR, Crichton RR. Iron, brain ageing and neurodegenerative disorders.
930 Nature Reviews Neuroscience. 2004 Nov; 5(11):863–873. doi: [10.1038/nrn1537](https://doi.org/10.1038/nrn1537).
- 931 **Zucca FA**, Segura-Aguilar J, Ferrari E, Muñoz P, Paris I, Sulzer D, Sarna T, Casella L, Zecca L. Interactions of
932 iron, dopamine and neuromelanin pathways in brain aging and Parkinson's disease. Progress in Neurobiol-
933 ogy. 2017 Aug; 155(C):96–119. <http://www.sciencedirect.com/science/article/pii/S030100821500101X>, doi:
934 [10.1016/j.pneurobio.2015.09.012](https://doi.org/10.1016/j.pneurobio.2015.09.012).